nature aging

Article

https://doi.org/10.1038/s43587-026-01107-0

Exoproteome of calorie-restricted humans identifies complement deactivation as an immunometabolic checkpoint reducing inflammaging

Received: 4 August 2025

Accepted: 9 March 2026

Published online: 13 April 2026

Check for updates

Manish Mishra[1,2,3,9], Hee-Hoon Kim[1,2,3,9], Yun-Hee Youm[1,2,3], Elsie Gonzalez-Hurtado[1,2,3], Konstantin Zaitsev[4], Tamara Dlugos[1,2,3], Irina Shchukina[4], Christy Gliniak[5], Eric Ravussin[6], Subhasis Mohanty[7], Albert C. Shaw[7,8], Philipp E. Scherer[5], Maxim N. Artyomov[4] & Vishwa Deep Dixit[1,2,3,8]

Caloric restriction (CR) extends lifespan across diverse organisms, but the effects of CR on human aging and on healthspan are only beginning to be uncovered. In this study, we applied proteomics to plasma samples collected longitudinally from participants achieving, on average, 14% CR over 2 years as part of the CALERIE trial. We identified that inhibition of the complement pathway is linked to lower inflammaging. In humans, the C3a/C3 ratio was significantly lowered by CR, thus reducing inflammation emanating from three canonical complement pathways. Furthermore, circulating C3a is elevated during aging in humans and in mice; we identified a non-senescent age-associated macrophage subset that expands in visceral fat as the predominant source. In macrophages, C3a-C3AR1 autocrine signaling via extracellular signal-regulated kinase (ERK) regulates age-related inflammation. Intra-adipose administration of a C3a-specific neutralizing antibody reduced inflammaging in mice. In addition, fibroblast growth factor 21 (FGF21) overexpression and deficiency of phospholipase A2 group VII (PLA2G7/lp-PLA2), which enhance lifespan and healthspan in mice, lowered C3a in aging. Thus, complement C3a reduction is a metabolically regulated inflammatory checkpoint that can be harnessed to attenuate inflammaging.

Aging entails the accumulation of damage-associated molecular patterns and chronic activation of the innate immune system, leading to time-dependent functional decline at the molecular, cellular and organismal levels, resulting in compromised health and death[1]. Therefore, identification of causal mechanisms that perturb homeostasis in aging and their successful targeting through dietary or pharmacological means are needed to promote the health of older adults and stave off chronic diseases. CR remains the most effective approach to extending the healthspan and lifespan of an organism[2–4]. Notably, phase 2 of the Comprehensive Assessment of Long-term Effects of Reducing Intake of Energy (CALERIE-II) clinical trial demonstrated that moderate 14% sustained CR for 2 years boosts the thymic and metabolic function while lowering inflammation in humans without inducing growth and reproduction tradeoffs[5–7]. However, the precise mechanisms underlying the beneficial effects of CR warrant further investigation.

A full list of affiliations appears at the end of the paper. e-mail: vishwa.dixit@yale.edu

The protective innate immune response of the host is central to the organism's survival. The complement system comprises evolutionarily conserved, ancient groups of proteins across different species, ranging from invertebrates to humans, that are key components of the protective innate immune response[8]. In addition to the documented role of the complement in opsonization and cell lysis, mounting evidence implicates complement proteins as important regulators of cellular functions, including tagging pathogens for elimination, recruitment of inflammatory cells and maintenance of tissue homeostasis[9–11]. Complement system activation, a cascade of more than 50 soluble or membrane-bound glycoproteins in humans, mainly involves three pathways: classical, lectin and alternative[12]. Importantly, complement activation, irrespective of the pathways involved, converges at the central component: complement component 3 (C3). Native C3 is thought to be biologically inactive, and its activation fragments exert multiple effector functions[11]. C3 is cleaved and activated by C3 convertase, producing byproducts C3a and C3b, which regulate inflammation[13]. Chronic inflammation, one of the major hallmarks of aging[14], drives most of the age-associated complications, suggesting the potential contribution of C3 and C3a. Elevated C3 concentrations are negatively correlated with longevity[15], but the mechanisms and causal role of C3-mediated complement activation in aging-associated loss of tissue function are unclear.

Lifespan is extended with CR while C3 concentrations increase in serum and organs of aged mice, including hippocampus and cortex, with C3 levels regulated, in part, by the NOD-, LRR- and pyrin domain-containing protein 3 (NLRP3) inflammasome[14,16–18]. Notably, the elevation of C3 and C3a are common signatures observed in aging[19,20]. In support of a strong association between aging and innate immune activation, recent proteomic analysis of human organ samples spanning approximately 50 years also identified complement and NLRP3 inflammasome activation among the top upregulated pathways[21]. Although recent reports have investigated the importance of the classical pathway protein C1q in aging-related phenotypes[22,23], the overall C3 derived from the lectin and the alternative pathways have been largely overlooked. In addition to the liver as a primary synthesis site[24], C3 is locally produced in the adipose tissue, including by adipocytes and macrophages[25–27]. Macrophage activation is well documented as a driver of age-associated inflammation or inflammaging[28]. However, the contribution and mechanisms of macrophages in age-associated C3-mediated inflammaging are still open questions.

In this study, using unbiased plasma proteomics, we discovered that 2 years of 14% CR reduced multiple complement proteins, including C3a, and related pathways in middle-aged healthy individuals, independent of body mass index (BMI). Consistent with its prolongevity effect, we found that CR slowed the adipose tissue proteomic aging clock in humans. By contrast, C3a expression increased with age in both humans and mice, and this activation is predominantly derived from visceral adipose tissue (VAT). Specifically, age-associated macrophage (AAM) subset in VAT was identified as the primary cellular source of age-related C3 production, and downstream signaling through the ERK pathway mediated the production of inflammatory cytokines in an autocrine manner. Accordingly, inhibition of C3a restrained inflammaging in aged mice. Moreover, we observed that the age-associated increase in C3a was partially blunted in long-lived FGF21 transgenic mice and CR-mimetic PLA2G7 knockout mice compared to wild-type controls. Together, our reverse translational approach reveals that the inhibition of the complement system is a promising, clinically relevant target to reduce inflammaging and prolong healthspan.

Results

CR rewires the directionality of the human exoproteome toward longevity pathways

To investigate the impact of 2 years of mild CR on the exoproteome of middle-aged healthy individuals, we performed an unbiased proteomics analysis using the SomaScan 7K assay on longitudinal plasma samples from 42 CALERIE participants from the Pennington Biomedical Research Center cohort in Baton Rouge, Louisiana, collected at baseline and after 2 years of 14% CR (Fig. 1a). Most participants in this cohort were in their 30s and 40s and were not obese (BMI < 30 kg m^{-2}), and they lost approximately 10% of their body weight after 2 years of CR (Fig. 1b and Extended Data Table 1). We detected a total of 7,029 proteins (SOMAmers) that passed quality control, and 262 proteins failed quality control (Fig. 1c and Supplementary Tables 1 and 2). Principal component analysis (PCA) showed that CR led to considerable changes in the plasma proteome of the participants (Extended Data Fig. 1a).

To explore the CR-induced proteomic shifts in detail, we performed differential expression analysis. We found that insulin-like growth factor-binding protein 2 (IGFBP2) was one of the top increased proteins after CR, whereas other IGFBPs remained unchanged except for IGFBP5, which was reduced (Fig. 1c,d and Extended Data Fig. 1b–h). IGFBP2 and IGFBP5 may impact mechanisms of aging by lowering the insulin growth factor 1 (IGF-1) bioavailability and are related to reduced mortality[29] and cellular senescence[30], respectively. Although the circulating IGF-1 concentration upon CR in our cohort was not different, these findings confirm the importance of reduced IGF-1 bioavailability, a mechanism identified from long-lived mice[31], for some beneficial effects of CR on aging in humans. In addition, CR significantly induced adiponectin levels but reduced leptin, fatty acid binding protein (FABP) 3 and 4 and growth hormone receptor levels, all of which are indicative of healthy aging (Fig. 1c,d and Extended Data Fig. 1i–m)[32–36]. Of note, even though the participants were healthy and did not have overt underlying inflammatory conditions, CR significantly decreased protein levels of complement components as well as other proinflammatory markers, such as C-reactive protein, tumor necrosis factor (TNF) and C-C motif ligand 1 (CCL1), but did not affect interleukin (IL)-1β and IL-6 levels in the plasma (Fig. 1d and Extended Data Fig. 1n–r).

A recent study established the Aging Atlas database, encompassing most of the hallmark pathways of aging based on previously published omics datasets[37]. We queried this database to examine the effects of CR on each aging hallmark pathway at the protein level. Interestingly, we found that none of the 12 aging hallmark pathways was increased, but more than half, including loss of proteostasis, genomic instability, deregulated nutrient sensing, nuclear factor-kappa B (NF-κB) signaling, stem cell exhaustion, cellular senescence and other aging-associated features, were significantly reduced by CR (Fig. 1e and Extended Data Fig. 1s). In particular, the prediction of upstream regulator analysis by Ingenuity Pathway Analysis (IPA) revealed that most of the NF-κB-regulated molecules were suppressed by CR (Fig. 1f), suggesting that plasma proteomics can reflect intracellular signaling hubs. These longitudinal analyses over 2 years of CR intervention in healthy individuals suggest reversal of some key aging hallmark signatures, particularly targeting both immune and metabolic pathways.

CR in humans slows adipose tissue proteomic aging clock

We next investigated the target organ(s) that may contribute to exoproteomic rewiring of aging hallmark pathways in humans after CR. To examine this, we used a recently developed algorithm, 'organage', which enables the estimation of organ-specific age using human plasma proteomics data[38]. This model first maps plasma proteins to putative organ sources based on organ-enriched expression features, defined as being more than four times higher in the organ of interest than in any other organ, in the Genotype-Tissue Expression project. It then uses these organ-enriched proteins to model organ-specific age and measures the gap between the chronological age and predicted age (Fig. 2a). Interestingly, based on these analyses, we found that CR significantly reduced the age gap only in adipose tissue but did not affect lung, kidney, artery, muscle and heart, and CR increased the age gap in the pancreas and intestine (Fig. 2b–i and Extended Data Fig. 2a–h).

Because this algorithm predicts organ age based on the association of protein expression with age rather than a causal relationship, we

https://doi.org/10.1038/s43587-026-01107-0

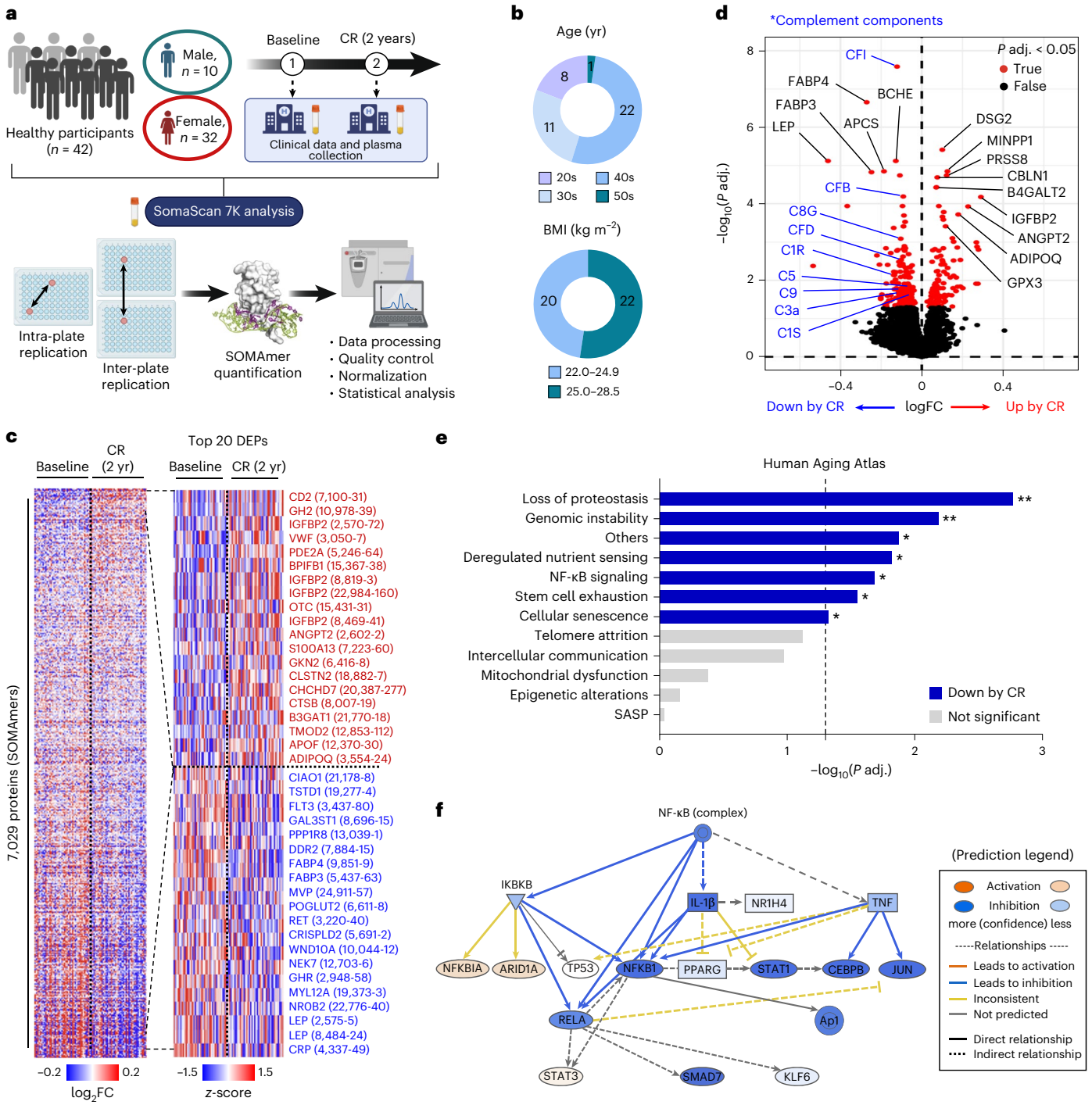

Fig. 1 | CR rewires the directionality of the human exoproteome toward longevity pathways. a–**f**, SomaScan 7K proteomics was performed in the plasma of healthy individuals at baseline and at 2 years after 14% CR ($n = 42$ per group, biological replicates). **a**, Schematic diagram of the overall study design. **b**, Age (top) and BMI (bottom) of participants. **c**, Heatmaps for all detected proteins ($n = 7{,}029$; left) and the top 20 increased or decreased differentially expressed proteins (DEPs) (right). **d**, Volcano plot for the plasma proteomics analysis. limma was used for differential expression analysis. **e**, CR-associated changes in 12 hallmarks of aging pathways were analyzed, and a scoring analysis of each pathway was performed. Adjusted *P* values are as follows: 0.002, 0.007, 0.013, 0.015, 0.021, 0.028, 0.048, 0.076, 0.107, 0.420, 0.691 and 0.923, from top to bottom. A two-tailed paired *t*-test was performed. **f**, Prediction of upstream regulator analysis for NF-κB in IPA. Most of the NF-κB signaling-related molecules were reduced by CR. Panel **a** created in BioRender; Dixit, V. https://biorender.com/uzr0jjv (2026). FC, fold change; *P* adj., adjusted *P* value; yr, years.

plotted all the organ-enriched proteins to examine the actual effects of CR on organ aging. For adipose tissue, we confirmed that CR beneficially modulated the adipose proteome, as shown in the differential expression analysis, with increased adiponectin and decreased leptin and FABP4 levels (Fig. 2k). Similarly, in the lung, CR significantly reduced CCL18 (Fig. 2l), which was implicated in pulmonary fibrosis[39]. Notably, although the estimation of proteomic age showed that the age gaps in the pancreas and intestine increased after CR, it also does not rule out reverse causality, as the significantly increased pancreas-enriched or intestine-enriched proteins after CR are implicated in tissue-protective roles, such as lipid digestion (PLA2G1B), protection from pancreatitis (CTRB1)[40], regulation of inflammatory bowel disease (REG1A)[41] and

https://doi.org/10.1038/s43587-026-01107-0

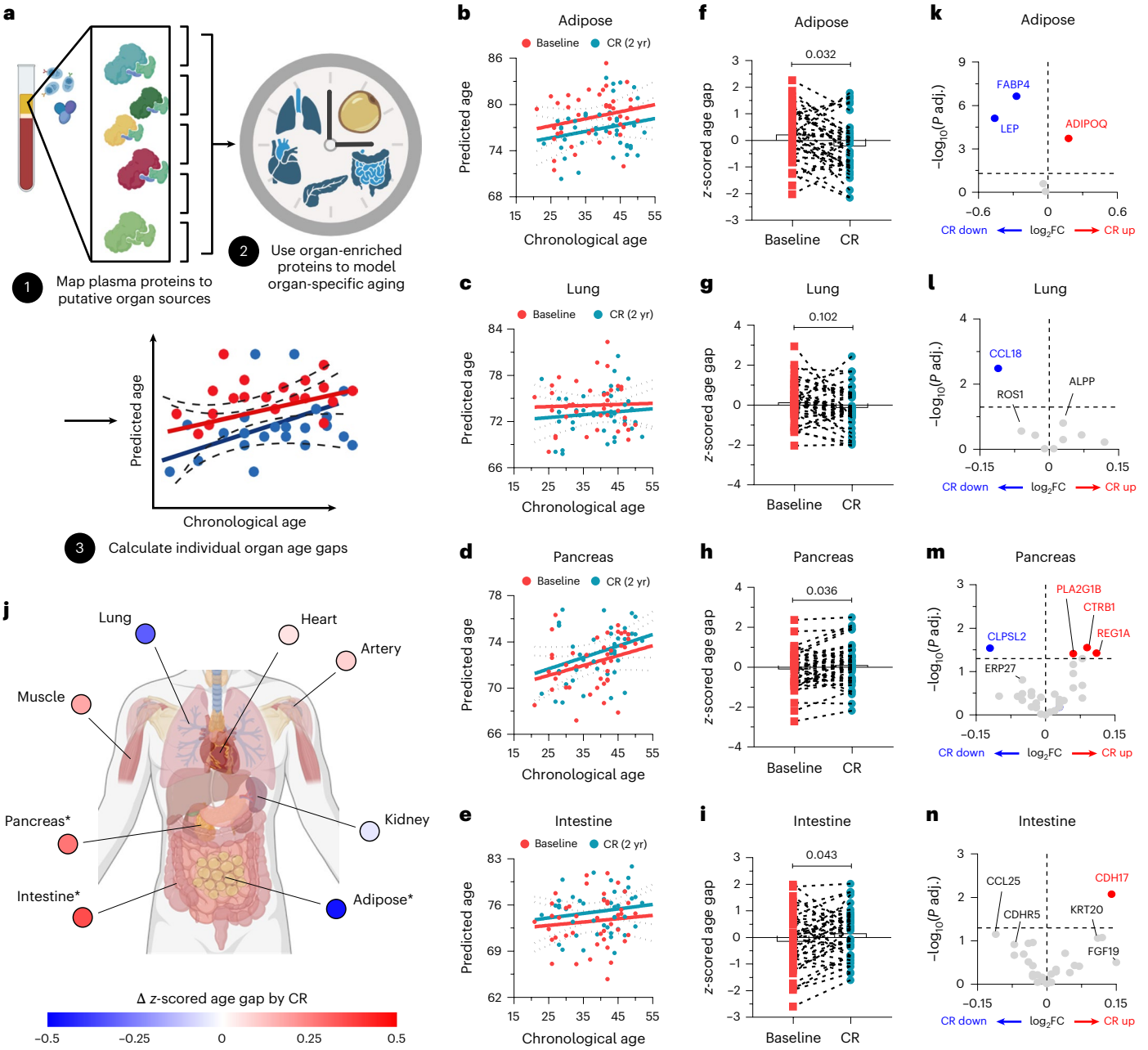

Fig. 2 | Mild and sustained CR in humans slow adipose tissue proteomic aging clock. a–n, Organ-specific aging signatures were analyzed based on the plasma proteome. **a**, Schematic diagram for the analysis pipeline. **b–e**, Linear regression analysis was performed to compare the predicted proteomic age before and after CR in adipose tissue (**b**), lung (**c**), pancreas (**d**) and intestine (**e**). **f–i**, Organ age gap was analyzed in adipose tissue (**f**), lung (**g**), pancreas (**h**) and intestine (**i**) ($n = 42$ per group, biological replicates). **j**, Summary of the changes in the delta *z*-scored organ age gap by CR. $^*P < 0.05$. **k–n**, Volcano plots for the organ-specific proteins in adipose tissue (**k**), lung (**l**), pancreas (**m**) and intestine (**n**). Paired two-tailed *t*-tests were performed, and exact adjusted *P* values are presented. Panels created in BioRender: **a**, Dixit, V. https://biorender.com/arhxxj3 (2026); **j**, Dixit, V. https://biorender.com/8qqlssz (2026).

supporting intestinal barrier function (CDH17)[42] (Fig. 2m,n). In addition, the kidney, artery and muscle did not show any significantly regulated proteins, and BMP10, important in cardiac development and function[43], was increased in the heart after CR (Extended Data Fig. 2i–l). However, the absence of change based on these in silico analyses may not fully capture the biology due to the lower sensitivities of detected protein features. Collectively, these data may suggest that CR is beneficial across various organs, with the most notable effects observed in the adipose tissue.

CR downregulates C3a level independently of BMI

To explore the specific mechanisms driving the benefits of CR, we performed pathway enrichment analysis with the plasma proteomics data using the Gene Ontology and Kyoto Encyclopedia of Genes and Genomes (KEGG) databases[44,45]. We found that CR upregulated pathways related to neuronal development, cardiac function and tissue remodeling (Fig. 3a). In addition, CR suppressed pathways involved in the regulation of lipid storage, positive regulation of IL-6 production and positive regulation of immune response (Fig. 3a). These results confirmed the previously reported immunometabolic advantages of CR[46–49]. Notably, the top downregulated pathways after CR were the 'complement and coagulation cascades' (Fig. 3a,b). Given that the expression levels of complement components increase with age and are implicated in various age-associated dysfunction[22,50,51], we delved deeper into CR-induced changes of each complement component.

We found that CR significantly reduced plasma levels of some early classical pathway-related components, such as C1s and C1r, but not C2,

C4 and C4b (Fig. 3c–g). In addition, CR also suppressed the expression levels of alternative pathway-related components, specifically CFB and CFD (Fig. 3h,i). A central event during complement activation is the cleavage of C3 into C3a and C3b, which further promotes inflammation and the formation of the membrane attack complex (MAC), respectively. Although C3 and C3b levels were not affected, both C3a and C3adesArg, a more stable form of C3a with the C-terminal arginine cleaved, were significantly reduced by CR (Fig. 3j–m). Furthermore, among the MAC components, C5 and C9 showed significant reductions after CR, whereas C6 and C7 levels remained unchanged, and C8 was not detected (Fig. 3n–q). Among these components, C1r, CFD and C3a were significantly reduced by CR in both sexes (Extended Data Fig. 3a–o). These results suggest that CR in humans suppresses the overall complement cascade rather than a specific pathway (Extended Data Fig. 4).

Because BMI has been reported to be associated with widespread changes in the circulating proteome in humans[52], we examined the association between BMI and the eight complement components (C1s, C1r, CFB, CFD, C3a, C3adesArg, C5 and C9) that were significantly reduced after CR. Of note, although the degrees of association were not strong, C1r, CFB, CFD and C5 showed significant positive correlations with BMI, indicating that the reduced expression levels of these molecules could be derived from weight loss after CR (Fig. 3r–u). By contrast, C1s, C3a, C3adesArg and C9 exhibited BMI-independent expression patterns (Fig. 3v–y). In sex-specific analysis, all eight complement components (C1s, C1r, CFB, CFD, C3a, C3adesArg, C5 and C9) in male participants were regulated by CR, independent of BMI, which could also be inferred from the low sample number (Extended Data Fig. 5a–h). However, in female participants, only C1s, C3a and C3adesArg were suppressed by CR in a BMI-independent manner (Extended Data Fig. 5a–h). Therefore, among C1r, CFD and C3a, whose expression levels were significantly reduced by CR in both sexes, C3a is the only component regulated independently of BMI. To further confirm and orthogonally validate that CR suppresses complement activation, we performed ELISA with archived plasma samples of CALERIE participants. We found that CR significantly reduced plasma C3a levels and the C3a/C3 ratio but not C3 levels (Fig. 3z). Thus, these data indicate that the inhibition of C3a might be a unique CR mimetic that can be harnessed to extend immune and metabolic healthspan.

Age-associated increase in C3 cleavage is unique to the VAT in mice

Given the data from the proteomics analysis of the CALERIE clinical trial, which established the relevance of the complement pathway in human metabolism, we used standard mouse models to test causality, source and the mechanistic role of C3a on organismal aging. First, we measured serum C3 and C3a levels in humans and mice to investigate the conservation of aging-associated dysregulation of the complement pathway. Cross-sectional analysis of young (age 21–36 years) and older (age ≥65 years) adults demonstrated a significant increase in C3 and C3a concentrations with age, whereas the C3a/C3 ratio was similar between the groups (Fig. 4a–d and Extended Data Fig. 6a,b). Furthermore, analyses of C57BL/6N mice from the National Institute on Aging (NIA) revealed that aging was associated with a significant elevation of C3a and the C3a/C3 ratio in both sexes of mice, whereas C3 was reduced (Fig. 4e–g and Extended Data Fig. 6c,d). These results indicate that both humans and mice exhibit an age-associated increase in complement abundance.

Next, we investigated the principal source of increased serum C3a levels observed in aged mouse through biochemical assays of various organs, including the liver, VAT, subcutaneous adipose tissue (SAT), brown adipose tissue (BAT), spleen and kidney from animals housed in different facilities, at either Yale University (C57BL/6J) or the NIA rodent colony (C57BL/6N). We were able to detect either C3 (185 kDa) or its cleaved forms, such as C3 α-chain (120 kDa), iC3b α-chain (68 kDa) and C3c α′-chain fragment 2 (39 kDa), in all tissues and samples analyzed. It was previously reported that the liver is a primary organ contributing to serum C3 levels[53]. However, upon aging, we observed only a modest increase in C3 and C3 α-chain liver expression levels in female mice, whereas male mice did not show any changes in C3 and its cleaved effectors with age (Fig. 4h–j). This suggests that the liver may not be a major contributing source of the aging-associated elevation of serum C3a levels. Similarly, although there were alterations in the levels of C3 and/or its cleaved molecules in some tissues, we could not find an increase in C3 cleavage in the SAT, BAT, spleen and kidney in either sex during aging (Extended Data Fig. 6e–l). Of note, we found that the age-associated increase in C3 cleavage was unique to the VAT in both sexes (Fig. 4k–m). In addition, the relative expression levels of C3 α-chain were the highest in the VAT among the analyzed tissues (Fig. 4n). Moreover, by analyzing Yale colony C57BL/6J male mice (likely possessing a different microbiome than the NIA rodent colony), we consistently observed that the VAT, and not the liver, was the major source of C3 cleavage during aging (Fig. 4h,k). This suggests that aging-associated complement dysregulation in VAT is not dependent on animal facility or husbandry-associated microbiota alterations that can impact immune-metabolic crosstalk.

Given that VAT is a major source of age-associated elevation of C3 and its cleaved products and previous reports linking the NLRP3 inflammasome with complement proteins[54,55], we asked whether the aged VAT-specific C3 cleavage requires NLRP3 inflammasome activation. We detected similar expressions of either C3 or its cleaved products in VAT from 24-month-old NLRP3-deficient mice and wild-type controls (Fig. 4o and Extended Data Fig. 6m), concluding that the unique C3 cleavage in aged VAT was NLRP3 independent. Together with the CALERIE proteomics data, which showed decreased proteomic age only in adipose tissue, these results demonstrate that VAT plays a unique and pivotal role in the age-associated immunometabolic dysregulation, possibly by contributing to the production of C3a.

Autocrine C3a signaling in adipose tissue macrophages regulates inflammaging

We next asked which complement pathway is involved in the elevation of C3a levels in the VAT of aged mice. By western blot analysis, we did not detect an increase in C1QA (classical pathway) or complement factor D (alternative pathway) during aging, and C2 (lectin pathway) was not detected in the VAT (Fig. 5a). Nevertheless, the ERK pathway, one of the downstream signaling pathways of the C3a receptor (C3AR1), was significantly activated with age in the VAT (Fig. 5a). Because previous studies reported C3 production by both adipocytes[25,27] and macrophages[26], we next sought to identify the cellular source of C3a within the VAT. To do this, we isolated mature adipocytes and the stromal-vascular-immune fraction (SVIF), which contains various cell types, including immune cells, from the VAT of 3-month-old and 24-month-old mice. In the mature adipocyte floating fraction, we could only detect C3c α′-chain fragment 2, but not C3 or C3 α-chain, and C3c α′-chain fragment was

Fig. 3 | CR in humans lowers complement C3a independently of BMI. a, Gene set enrichment analysis for databases GO BP and KEGG. Only significant pathways (adjusted $P < 0.05$) are shown with the exact adjusted P value. limma was used for statistics. **b**, Enrichment plots for complement and coagulation cascades from the KEGG database and regulation of lipid storage from GO BP. limma was applied for statistics. **c**–**q**, ANML normalized expression values for the C1s (**c**), C1r (**d**), C2 (**e**), C4 (**f**), C4b (**g**), CFB (**h**), CFD (**i**), C3 (**j**), C3a (**k**), C3adesArg (**l**), C3b (**m**), C5 (**n**), C6 (**o**), C7 (**p**), and C9 (**q**) ($n = 42$ per group, biological replicates). **r**–**y**, Linear regression analysis was conducted to examine the correlation between BMI and C1r (**r**), CFB (**s**), CFD (**t**), C5 (**u**), C1s (**v**), C3a (**w**), C3adesArg (**x**), or C9 (**y**). **z**, Plasma C3 and C3a levels were measured by ELISA, and the C3a/C3 ratio was calculated ($n = 20$ per group, biological replicates). For **c**–**q** and **z**, paired two-tailed t-tests were performed, and adjusted P values (**c**–**q**) or P values (**z**) are presented. GO BP, Gene Ontology Biological Process; NES, normalized enrichment score.

https://doi.org/10.1038/s43587-026-01107-0

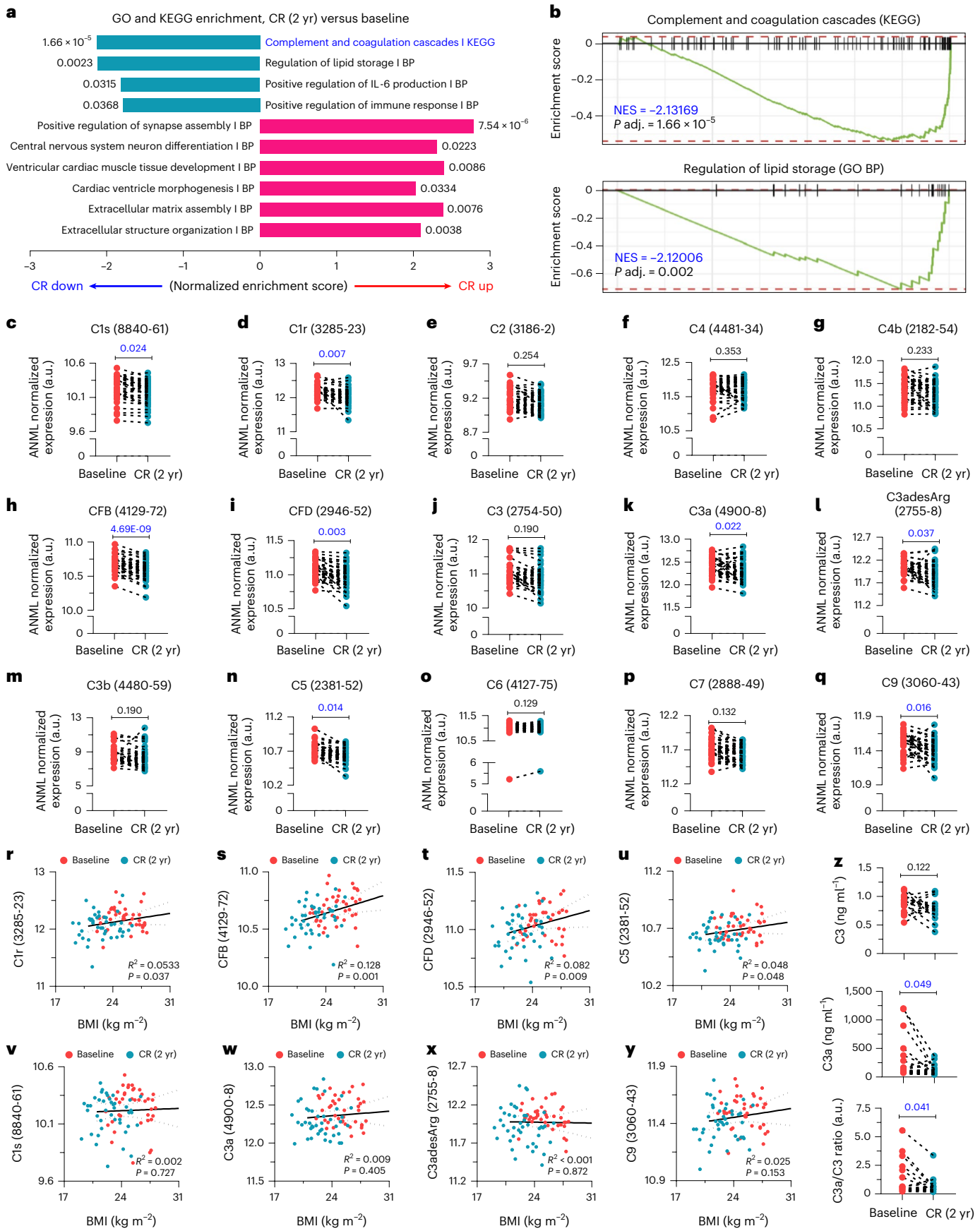

increased with age (Fig. 5b and Extended Data Fig. 7a). However, a caveat of this finding is that floating adipocyte fractions are typically contaminated with lipid-containing macrophages, potentially accounting for C3 concentrations. Notably, we observed all forms of C3 and its cleaved products in the SVIF, where C3 α-chain and C3c α′-chain fragment 2 were significantly increased with age (Fig. 5c and Extended Data Fig. 7b). Moreover, although we did not find age-associated changes in C1QA and CFD in whole VAT, there was a tendency for an increase in both proteins in the SVIF with age, along with ERK activation (Fig. 5c and Extended Data Fig. 7b). These results suggest that C3 cleavage in VAT during aging is predominantly of non-adipocyte origin.

To gain further insight into the cellular source of C3, we analyzed our previously reported single-cell RNA sequencing (scRNA-seq) data of VAT-resident immune cells[56]. Interestingly, we found that both *C3* and *C3ar1* expressions were enriched in adipose tissue macrophages (ATMs) among the 15 different resident immune cell types (Fig. 5d). A comprehensive subtyping analysis of VAT-resident ATMs via scRNA-seq[57] revealed that, whereas *C3ar1* expression was ubiquitously observed across various ATM subsets, AAMs, which predominantly emerge in old mice, primarily accounted for the age-related elevation in *C3* expression (Fig. 5e,f and Extended Data Fig. 7c,d). Notably, the AAMs (CD45$^+$F4/80$^+$CD11b$^+$CD169$^-$CD11c$^-$FOLR2$^-$CD38$^+$) did not exhibit elevated levels of *Cdkn1a* and *Cdkn2a* and did not show a significant reduction of *Lmnb1* in aged mice, which are considered to be some of the canonical markers of cellular senescence[57] (Fig. 5g). This suggests that AAM subtypes of VAT-resident macrophages, which are not senescent, are the predominant source of elevated C3 and associated inflammatory proteins during aging. In addition, these data underscore that the tissue-resident dysfunctional macrophages are the likely source of inflammaging instead of senescent cells that are hypothesized to cause aging through senescence-associated secretory phenotype (SASP), a set of non-specific proteins primarily produced by immune cells[58–60].

Further analysis of age-associated changes in the expression levels of these genes in ATMs through RNA-seq[61], which has greater sensitivity than scRNA-seq, showed that both *C3* and *C3ar1* were significantly increased during aging independent of NLRP3 inflammasome (Fig. 5h), suggesting autocrine activation of C3 in ATMs during aging. To orthogonally confirm the age-associated increase in C3 expression in ATMs at the protein level, we performed flow cytometry analysis (Extended Data Fig. 7e). We observed that higher frequency of F4/80$^+$CD11b$^+$ ATMs in aged mice expressed C3 compared to young mice of both sexes, whereas cells in the F4/80$^-$CD11b$^+$ non-macrophage fraction did not exhibit any difference with aging (Fig. 5i,j).

After confirming that ATMs are key contributors to the VAT-specific age-associated increase in C3a production, we sought to further understand the signaling mechanisms and physiological functions of observed changes. To model this, we used bone marrow-derived macrophages (BMDMs) from young male mice and exposed them to C3a. We found that recombinant C3a treatment induced early ERK activation and time-dependent signal transducer and activator of transcription 3 (STAT3) activation in BMDMs, suggesting that BMDMs possess the machinery to signal to exogenous C3a (Fig. 5k). In addition, we observed that STAT3 activation by C3a treatment was ERK dependent, as pretreatment with an ERK inhibitor also suppressed STAT3 activation in BMDMs (Fig. 5l). By contrast, pretreatment with a STAT3 inhibitor did not affect ERK activation (Fig. 5l), suggesting that ERK activation in response to complement C3a is an upstream signaling event. Consistent with these results and the previously reported proinflammatory function of the C3a signaling pathway in macrophages[62], we found that C3a treatment induced IL-1β and IL-6 production by BMDMs in an ERK-dependent but STAT3-independent manner (Fig. 5m).

Our previous work found that ATMs actively control lipid metabolism of adipocytes during aging[61]. To determine whether C3a signaling in macrophages impacts adipocyte lipolysis, we performed ex vivo experiments with VAT explants from 3-month-old and 24-month-old mice, treating them with C3a in addition to lipopolysaccharide (LPS) to model in vivo inflamed environments. We found that C3a and LPS treatment did not affect lipolysis in VAT explants from either 3-month-old or 24-month-old mice (Fig. 5n). However, compared to 3-month-old mice, we found reduced lipolysis in complement-exposed VAT explants from 24-month-old mice (Fig. 5n). Collectively, these data demonstrate that C3a is produced by ATMs and impairs adipose function by increased age-associated inflammation in an autocrine manner.

Inhibition of complement C3a and C3 reduces inflammaging

The above findings guided us to investigate whether inhibition of C3a could mimic the immunometabolic benefits of CR in vivo. For this purpose, we used a C3a-specific neutralizing antibody (α-C3a), which was previously used in mice[63–65]. To further validate the efficacy and specificity of anti-C3a antibody, purified F4/80$^+$ ATMs from young and aged mice were treated with anti-C3a antibody or isotype control, followed by recombinant C3a activation (Fig. 6a). In ATMs from young mice, we found that anti-C3a antibody-only treatment did not regulate the production of IL-1β at steady state (Fig. 6b). However, once activated by recombinant C3a protein, ATMs released significantly more IL-1β, which was partially but significantly suppressed by pretreatment of anti-C3a antibody (Fig. 6b). In addition, consistent with our data that AAMs in VAT of aged mice produced more C3, the baseline IL-1β production was higher in ATMs sorted from aged mice compared to young mice, which was suppressed by C3a neutralization (Fig. 6b,c). Moreover, as seen in ATMs from young mice, the anti-C3a antibody significantly reduced IL-1β production of C3a-stimulated cells from aged mice (Fig. 6c).

Based on this experimental evidence, we next performed in vivo experiments with aged (20-month-old) mice randomly allocated to isotype or anti-C3a antibody groups. To neutralize the effects of elevated C3a in VAT, where autocrine C3a-C3AR1 signaling in ATMs instigates inflammation, we administered antibodies through intra-adipose route in aged mice (Fig. 6d). Because the intra-adipose delivery of anti-C3a antibody (or isotype control) requires abdominal surgery to extrude visceral fat, the mice were injected once and euthanized after 3 days. Despite short-term VAT-specific delivery, serum C3a levels showed a reduced trend by anti-C3a treatment in comparison to the isotype controls, whereas serum C3 levels and the C3a/C3 ratio were similar between the groups (Fig. 6e and Extended Data Fig. 8a,b). In addition, we observed a significant suppression of ERK activation in the anti-C3a antibody group (Fig. 6f), confirming that the C3a-neutralizing antibody inhibited the downstream effects of C3a. Consistent with these data, anti-C3a antibody treatment of aged mice significantly lowered

Fig. 4 | Aging increases C3 cleavage with VAT as a major source. a, Schematic diagram for C3 cleavage. **b**–**d**, Human serum samples were analyzed for C3 (**b**) and C3a (**c**) ELISA, and the C3a/C3 ratio (**d**) was calculated in both sexes (**a**; $n = 14$ for 21–36 years and $n = 11$ for >65 years, biological replicates). Box plots indicate minimum to maximum. **e**–**g**, Mouse serum samples were analyzed for C3 (**e**) and C3a (**f**) ELISA, and the C3a/C3 ratio (**g**) was calculated in both sexes ($n = 12$ per group, biological replicates). Box plots indicate minimum to maximum. **h**–**j**, C3 western blot analysis of mouse liver. **h**, Representative blots for C3. **i**, Densitometry analysis of male mice ($n = 9$ for 3-month-old and $n = 10$ for 24-month-old, biological replicates). **j**, Densitometry analysis of female mice ($n = 4$ for 3-month-old and $n = 6$ for 24-month-old, biological replicates). **k**–**m**, C3 western blot analysis of mouse VAT. **k**, Representative blots for C3. **l**, Densitometry analysis of male mice ($n = 9$ for 3-month-old and $n = 11$ for 24-month-old, biological replicates). **m**, Densitometry analysis of female mice ($n = 4$ for 3-month-old and $n = 6$ for 24-month-old, biological replicates). **n**, Representative blots for C3 in the indicated tissues of 24-month-old mice. Each lane indicates a different mouse. **o**, Representative blots for C3 in 24-month-old WT ($n = 3$, biological replicates) and NLRP3$^{-/-}$ ($n = 5$, biological replicates) mice. Unpaired two-tailed *t*-tests were performed, and exact *P* values are presented. Data are presented as mean ± s.e.m. mo, months; WT, wild-type; n.d., not detected.

https://doi.org/10.1038/s43587-026-01107-0

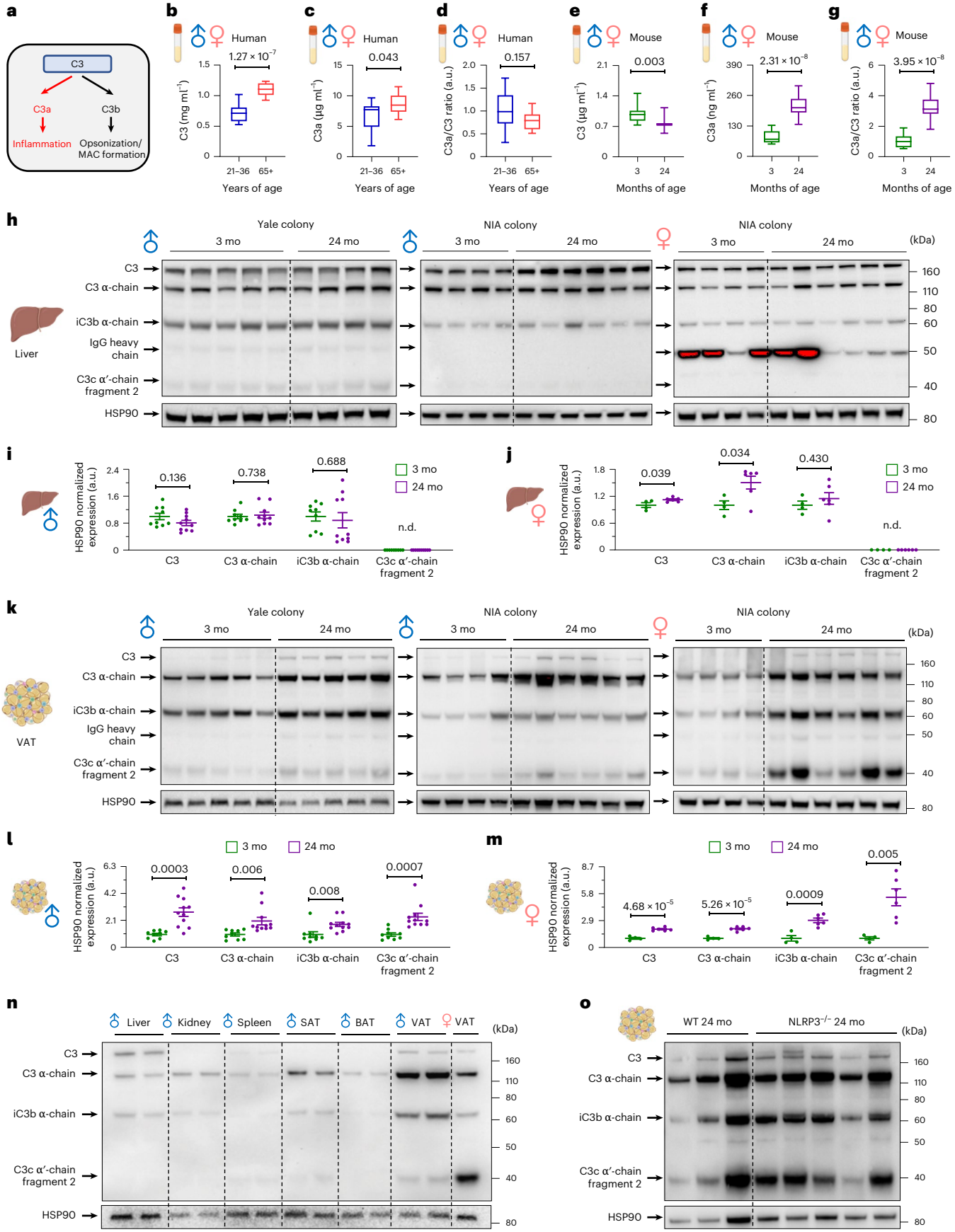

IL-1β and monocyte chemoattractant protein 1 (MCP-1), whereas IL-6 showed a trend of reduction and TNF remained unchanged (Fig. 6g–i and Extended Data Fig. 8c). To examine the impact of C3a neutralization on immune cell composition of aged VAT, we performed multicolor flow cytometry analysis (Extended Data Fig. 8d,e). We found that intra-adipose injection of anti-C3a antibody significantly reduced the frequencies of total ATMs, Ly6C$^+$ monocytes, regulatory T (T_{reg}) cells and CD4 T cells while elevating the frequencies of M2-like antiinflammatory ATMs and did not affect M1-like proinflammatory ATMs, aged adipose B cells, CD8 T cells, natural killer cells and neutrophils (Fig. 6j–n and Extended Data Fig. 8f–j). These results might indicate that a selective inhibition of C3a in VAT could be an actionable target that restrains inflammaging. Notably, AMY-101, which is a selective C3 inhibitor in humans and has recently concluded a phase 2a clinical trial for patients with periodontal inflammation[66,67], has low efficacy in mice[68] and might elicit off-target effects at high doses (Supplementary Fig. 1a–c and Supplementary Note).

Given that FGF21, PLA2G7 and secreted protein acidic and cysteine-rich (SPARC) are regulated by CR and control healthspan by restraining inflammaging[5,6,69–71], we investigated the link between the C3 cleavage and healthy aging in the VAT of aged mice overexpressing FGF21 and lacking PLA2G7 and SPARC. Of note, 24-month-old FGF21 transgenic (FGF21-Tg) and PLA2G7 knockout mice exhibited significantly reduced C3 cleavage compared to age-matched controls (Fig. 6o,p). However, 16-month-old SPARC knockout mice showed similar expression of C3 and its cleaved forms to control mice (Extended Data Fig. 9a), suggesting that the prolongevity effects of FGF21 overexpression and PLA2G7 reduction may involve a reduction in C3 cleavage. By contrast, the SAT from 18-month-old adipocyte-specific FGF21-overexpressed (ADN-iFGF21-Tg) mice did not show any reduction in C3 levels (Extended Data Fig. 9b), highlighting that C3 activation is specific to the VAT. Collectively, these data suggest that the inhibition of C3 extends healthspan by regulation of immunometabolic mechanisms in aged mice.

Discussion

CR, the most effective non-pharmacological prolongevity intervention, has been shown to improve healthspan and extend lifespan in many species, including rodents and primates[5,6,16]. In the present series of studies, including unbiased proteomics analysis of a human CR clinical trial, we propose that targeting C3 activation could be a CR mimetic and should be tested as an intervention strategy for improving healthspan and potentially lifespan. Under homeostatic conditions, inflammatory cues result in complement activation and resolve the damage. However, sustained elevation of C3a is detrimental to longevity, and a reduction in C3 levels has been shown to improve age-related kidney dysfunction in mice and extend lifespan in *Caenorhabditis elegans*[18,72]. Therefore, our findings suggest that increased age-associated complement activation can potentially be targeted to improve health outcomes in older adults.

Aging is associated with increased visceral adiposity, a hallmark of aging, characterized by homeostatic perturbations, weakened stress resilience, metabolic decline and chronic inflammation[73]. Among the primary goals of translational geroscience research is to delineate mechanistic insights of aging and to discover or target the pathways with interventions that mitigate functional decline in aging. To achieve this goal, recent discoveries have established genetically manipulated FGF21 and PLA2G7 mouse models that exhibit extended healthspan[5,74,75], and finding the common mechanistic targets across these established interventions could accelerate progress in geroscience. Our studies, based on human CR intervention data, identified that adipose tissue complement deactivation is a common inflammaging checkpoint shared among non-pharmacological and genetic interventions. Given that many complement inhibitors are clinically being tested and complement activation has been implicated in multiple aging-related diseases, including Alzheimer's disease, age-related macular degeneration and osteoarthritis[76], pharmacological inhibition of C3 activation by FDA-approved inhibitors could be a feasible approach to delay systemic physiological and functional declines during aging.

Indeed, in line with reduced complement proteins in the CALERIE participants, we found that pharmacological inhibition of C3a improved age-related inflammation in aged mice. However, one potential pitfall in the long-term clinical use of C3 inhibitors is the existence of non-canonical intracellular C3 signaling pathways, which regulate essential cellular processes, including energy metabolism, lipid metabolism, cell survival and efferocytosis[53]. Given that a complement cascade is required for protection against infections and our studies are performed in a standard specific pathogen-free condition, careful clinical trials are required to determine the most efficient and safest dose of C3a inhibitors for long-term clinical use that restores age-related elevated complement activation to normal baseline levels.

Of note, our data implicate VAT as a major contributor to age-associated increased complement activation-mediated inflammation. In addition, we also report that ATMs are central in displaying age-associated complement cleavage by using ERK-dependent STAT3 activation. However, owing to the limited durability of neutralizing antibody experiments, we could not provide a causal relationship between C3a inhibition and CR-mediated healthspan extension, and serum complement levels were statistically inconclusive. In addition, how macrophage-specific C3 regulates the adipose tissue microenvironment during the aging process requires further investigation with genetically modified mouse models. Because complement proteins are involved in multiple physiological events and C3AR1 is present in many cell types, whether macrophage-specific C3 effector functions rely more on autocrine, paracrine or endocrine signaling during the aging process requires genetically modified aged animals for further mechanistic insights.

Although we included as many individuals as possible for exoproteome analysis, a larger cohort analysis would be helpful to detect more subtle changes that could not be captured in the present study. In addition, future studies are required to delineate the tissue-specific effects of CR that are uncoupled from weight loss in regulating inflammaging.

Fig. 5 | Autocrine C3a signaling in ATMs regulates inflammaging. **a**, Representative western blot with densitometry analysis ($n = 5$ per group, biological replicates). **b**,**c**, Representative western blot analysis of VAT adipocytes (**b**) and VAT SVIF (**c**) ($n = 5$ per group, biological replicates). **d**, *C3* and *C3ar1* expression in scRNA-seq of mouse VAT SVIF. **e**–**g**, scRNA-seq analysis of VAT-resident macrophages was performed in 2-month-old and 22-month-old mice. *C3* expression by age (**e**) and by macrophage subtypes (**f**). **g**, *Cdkn1a*, *Cdkn2a* and *Lmnb1* levels in AAMs. **h**, *C3* and *C3ar1* expression levels in bulk RNA-seq analyses of VAT ATMs ($n = 3$ per group, biological replicates). **i**,**j**, C3 expression in F4/80$^+$CD11b$^+$ VAT ATMs and F4/80$^-$CD11b$^+$ non-macrophage fraction of male (**i**; $n = 6$ for 4-month-old and $n = 3$ for 23-month-old, biological replicates) and female (**j**; $n = 5$ for 3-month-old and $n = 5$ for 22-month-old, biological replicates) mice. **k**, Representative western blot analysis of mouse BMDMs treated with recombinant C3a. **l**,**m**, BMDMs were pretreated with vehicle (DMSO), ERK inhibitor (U0126) or STAT3 inhibitor (S3I-201), followed by C3a, and subjected to western blot analysis (**l**) or ELISA (**m**; $n = 3$ per group, biological replicates). **n**, VAT explants were treated with either vehicle (VEH) or LPS and C3a, and free fatty acid levels were measured in the culture supernatant ($n = 6$ for young VEH, $n = 6$ for young LPS+C3a, $n = 5$ for old VEH and $n = 6$ for old LPS+C3a, biological replicates). Unpaired two-tailed *t*-tests (**a**,**i**,**j**) or one-way ANOVA with multiple comparisons (**h**,**m**,**n**) were performed, and exact *P* values are presented. Data are presented as mean ± s.e.m. cATM, cyclic ATM; DC, dendritic cell; FSC-A, forward scatter area; hrs, hours; IAM, interferon-associated macrophage; KO, knockout; LAM, lipid-associated macrophage; MP, macrophage; NAM, nerve-associated macrophage; NK, natural killer; tSNE, *t*-distributed stochastic neighbor embedding; UMAP, uniform manifold approximation and projection; VAM, vascular-associated macrophage; cDC, conventional dendritic cell; pDC, plasmacytoid dendritic cell; ILC, innate lymphoid cell.

https://doi.org/10.1038/s43587-026-01107-0

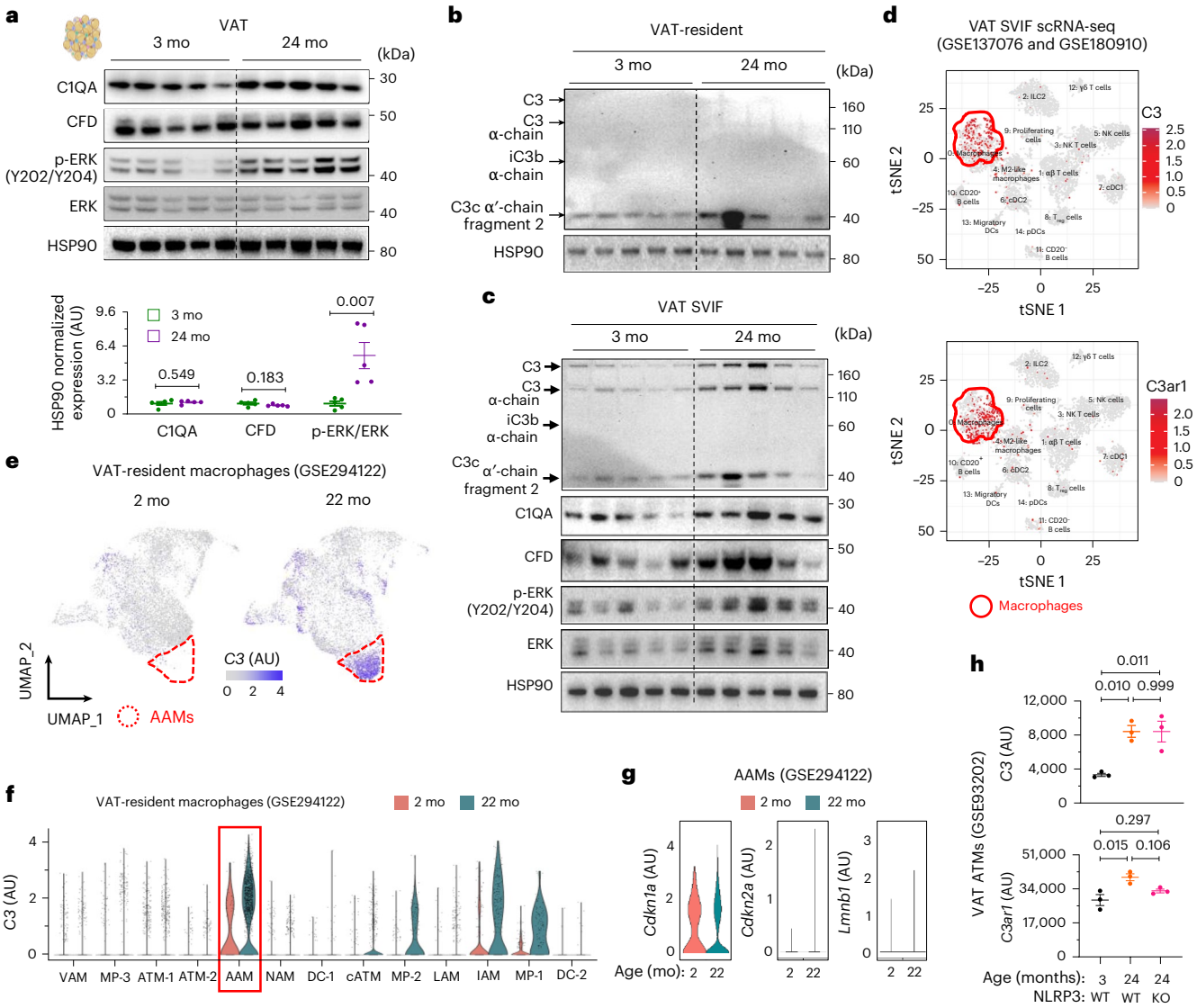

https://doi.org/10.1038/s43587-026-01107-0

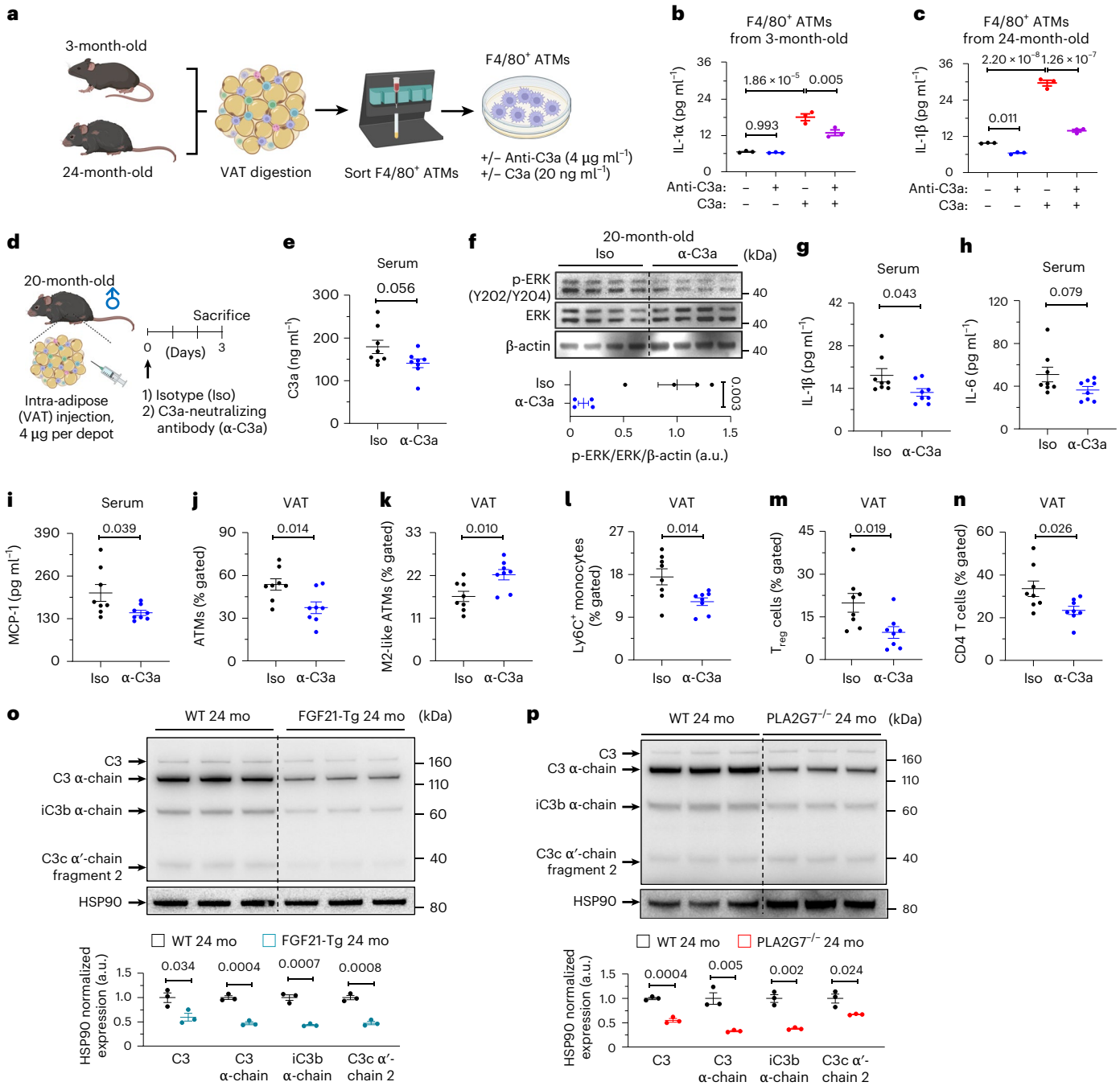

Fig. 6 | VAT-specific inhibition of C3a restrains inflammaging. a, Schematic diagram of in vitro validation of anti-C3a antibody. **b**,**c**, F4/80$^+$ ATMs were pretreated with anti-C3a antibody (4 μg ml^{-1}) for 1 hour, followed by C3a (20 ng ml^{-1}). IL-1β levels in culture supernatants were measured in young (**b**) or aged (**c**) mice ($n = 3$ per group, biological replicates). **d**–**n**, Aged (20-month-old) male mice were randomly allocated, and 4 μg of either isotype (Iso) or anti-C3a antibody (α-C3a) was directly injected into both VAT depots. Mice were euthanized after 3 days ($n = 8$ per group, biological replicates). **d**, Schematic diagram. **e**, Serum C3a levels. **f**, Representative western blot for ERK activation with densitometry analysis ($n = 4$ blots per group, biological replicates). **g**–**i**, Serum IL-1β (**g**), IL-6 (**h**) and MCP-1 (**i**) levels. **j**–**n**, Flow cytometry analysis of the frequencies of VAT ATMs (**j**), M2-like ATMs (**k**), Ly6C$^+$ monocytes (**l**), T_{reg} cells (**m**) and CD4 T cells (**n**). **o**,**p**, Representative C3 western blot analysis of the VAT of 24-month-old WT and FGF21-Tg (**o**) and 24-month-old WT and PLA2G7$^{-/-}$ (**p**) mice ($n = 3$ per group, biological replicates). Unpaired two-tailed *t*-tests were performed, and exact *P* values are presented. Data are presented as mean ± s.e.m. Panels **a** and **d** created in BioRender; Dixit, V. https://biorender.com/2jdpq2w (2026).

Additionally, investigations into the interaction of obesity and aging may help to broaden understanding of the importance of complement activation in inflammaging.

Given that an FDA-approved C3 inhibitor drug (pegcetacoplan) is currently prescribed for age-related macular degeneration and other hematological diseases[77], future clinical trials for repurposing C3 inhibitors in aging are required for the development of pharmacological interventions to potentially extend healthspan and lifespan. In summary, our reverse translational approach demonstrates that deactivation or reduction of complement serves as an inflammaging checkpoint and highlights the pivotal role of maintaining macrophage and adipose tissue homeostasis during aging. Our data

support immune antagonistic pleiotropy theory, where complement proteins that evolved for host defense and allow early-life survival cause detrimental effects upon aging.

Methods

Human participants

All clinical studies were performed under approved guidelines by the institutional review board at Pennington Biomedical Research Center or Yale University, with written informed consent from participants[5,71]. The samples used for the plasma proteomics were from the volunteer participants of the CALERIE-II study, a multicenter and randomized controlled trial. Plasma samples were collected at baseline and after 2 years of 14% CR from a total of 42 middle-aged, non-obese healthy individuals. All the detailed characteristics of the participants are listed in Extended Data Table 1. Serum samples of a total of 17 young adults (21–30 years) and 23 older adults (>65 years) were collected at Yale Hospital to quantify the C3.

Mice

The Yale Institutional Animal Care and Use Committee reviewed and approved all animal procedures. Young (3–5 months old) and aged (20–24 months old) wild-type male and female C57BL/6J mice were purchased from The Jackson Laboratory, and C57BL/6N mice were provided by the NIA Aged Rodent Colony. All mice used in this study were maintained in a ventilated cage rack in specific pathogen-free conditions at Yale School of Medicine. Mice were group housed, fed a standard vivarium chow diet and water ad libitum and maintained under a regular 12-hour light/dark cycle with maintained temperature (approximately 22 °C) and humidity (60%). C57BL/6N mice were mainly used for the mouse experiments, otherwise stated in the figure. The sex of the mice used is represented in each figure and legend. For C3a neutralization experiments, 20-month-old C57BL/6N male mice were randomly assigned to an isotype or an anti-C3a group. Four micrograms of antibody was injected into each depot of VAT, and mice were euthanized after 3 days.

SomaScan 7K assay

Plasma samples of CALERIE participants ($n = 42$) were subjected to the SomaScan 7K assay. The initial assay and normalization followed SomaLogic's pipeline. In brief, SomaScan assay data are initially normalized using hybridization controls to reduce variation within the run caused by readout steps. Subsequently, median signal normalization is performed across pooled calibrator replicates within the run to address within-run technical variations in the calibrator signals before employing them for scaling calculations. The ratios of the reference value to the median of replicates for each SOMAmer are calculated and decomposed into two components: plate scale, representing the median ratio, and calibration scale, representing the recalculated set of scale factors specific to each SOMAmer reagent. The plate scale adjusts for overall signal intensity differences between runs, and calibration adjusts for reagent-specific assay differences between runs. Median signal normalization is conducted using adaptive normalization by maximum likelihood (ANML) for plasma.

For proteomic expression, we used ANML normalized values provided by SomaLogic. The values were $\log_2$ transformed, and proteins that failed internal SomaScan quality control were removed. All the SOMAmers that failed quality control are listed in Supplementary Table 2. To identify proteins differentially expressed under CR, we fitted linear models using the limma R package (version 3.56.2)[78], including donor as a blocking factor for paired testing.

For hallmarks of aging analysis, the list of genes associated with each aging hallmark pathway was obtained from the Human Aging Atlas[37]. Heatmaps were generated using the z-scored $\log_2$ fold change of ANML normalized values. Scoring analysis was conducted by calculating the average value of all the genes involved in each specific pathway. Statistical significance was assessed using a two-tailed paired t-test, and adjusted P values were used. The proteomic age of each organ was estimated using the 'organage' package[38]. Input data included SOMAmer ID and ANML normalized values in relative fluorescence units (RFU) provided by SomaLogic. The calculated z-scored age gaps from the 'organage' package were used to predict whether the aging of each organ was accelerated or delayed after CR.

Pathway enrichment of the resulting protein signatures was performed with the fgsea R package (version 1.26.0)[79], using the limma t-statistic as the ranking metric. Volcano plots were generated with ggplot2 (version 3.5.1). For PCA, expression values were first normalized via variance stabilizing normalization using the vsn R package (version 3.68.0)[80], after which PCA was performed with the base R prcomp function and visualized in ggplot2 (version 3.5.1). R version 4.3.0 was used for all analyses. The ANML normalized values for plasma proteomics are provided in Supplementary Table 1 and are publicly available at Zenodo (https://doi.org/10.5281/zenodo.18805277)[81].

IPA

The fold change and P values from the SomaScan 7K assay were used as inputs for IPA. The upstream regulator analysis for NF-κB and the canonical pathway analysis for the 'complement system' were conducted according to the manufacturer's instructions.

ELISA and Luminex

The serum protein levels of C3 and C3a in humans (Hycult Biotech) and mice (C3, Abcam; C3a, Thermo Fisher Scientific) were assessed using ELISA in both sexes. For C3a neutralization experiments, serum IL-1β, IL-6, TNF and MCP-1 levels were analyzed by the Mouse Quantikine ELISA Kit from R&D Systems.

Immunoblot

Western blots were carried out on the whole-cell lysates from liver, kidney, spleen, SAT, BAT and VAT collected from young and old mice of both sexes, which were homogenized in RIPA buffer containing phosphatase and protease inhibitor cocktail. Complement C3 (Abcam, ab200999), C1QA (Abcam, ab155052), Factor-D/Adhipsin (R&D Systems, MAB5430-SP), p-STAT3 (Cell Signaling Technology, 9145), total STAT3 (Cell Signaling Technology, 4904), p-Erk (Cell Signaling Technology, 4377S), total Erk (Cell Signaling Technology, 4695S), HSP-90 (Proteintech, 60318-1-Ig) and β-actin (Cell Signaling Technology, 4967L) as primary antibodies and HRP-conjugated goat anti-rabbit or anti-mouse as secondary antibodies were used to detect proteins using the ChemiDoc MP Imaging System (Bio-Rad).

Adipose tissue digestion and flow cytometry analysis

VAT was digested with the digestion buffer containing 3% BSA, 8 mg ml^{-1} Collagenase II, 1.2 mM $CaCl_2$, 1.0 mM $MgCl_2$ and 0.8 mM $ZnCl_2$ in HBSS for 40 minutes in a 37 °C water bath with 200 r.p.m. agitation. After the digestion, the samples were centrifuged for 5 minutes at 500g at 4 °C. The top adipocyte layer was discarded carefully with suction, and the pellets were resuspended in 5 ml of complete RPMI media, followed by filtering with a 100-µm cell strainer. Cells were then centrifuged one more time for 5 minutes at 500g at 4 °C. After discarding the supernatant, pellets were resuspended in 1 ml of RBC lysis buffer and quenched with 5 ml of complete RPMI media after 2 minutes. Samples were filtered with a 70-µm cell strainer, followed by centrifugation for 5 minutes at 500g at 4 °C. Pellets containing SVIF were counted and used for flow cytometry analysis.

SVIF cells were stained as follows. Cells were first incubated with ViaKrome 808 Fixable Viability Dye (Beckman Coulter, C36628) or Live/Dead Fixable Aqua Dead Cell Stain Kit for 405-nm excitation (Thermo Fisher Scientific, L34957) and further stained with Fc receptor (CD16/32) blocking (Invitrogen, 14-0161-86) for 10 minutes. After that, cells were incubated with the surface antibodies. For analyzing

T_{reg} cells, cells were permeabilized and fixed with eBioscience Foxp3/Transcription Factor Staining Buffer Set (Thermo Fisher Scientific, 00-5523-00) according to the manufacturer's instructions after surface staining. Samples were acquired on a BD Biosciences LSR II or Symphony instrument, and data were analyzed using FlowJo software (TreeStar). All the antibodies used are listed in the reporting summary.

Ex vivo lipolysis

Young and old VAT explants (approximately 15 mg) were collected in a 96-well plate and cultured in lipolysis buffer with 500 ng ml^{-1} LPS and 40 ng ml^{-1} recombinant C3a for 4 hours at 37 °C. Free fatty acid assay (Sigma-Aldrich) was performed according to the manufacturer's instructions.

BMDM culture

BMDMs were prepared from male mice between 8 weeks and 12 weeks of age as previously described[6]. BMDMs were treated with LPS (500 ng ml^{-1}) before recombinant C3a protein (20 ng ml^{-1}) treatment. For blocking ERK or STAT3 activation, BMDMs were treated with ERK inhibitor U0126 (2.5 μM) or STAT3 inhibitor S3I-201 (25 μM) for 1 hour before LPS or C3a stimulation.

F4/80$^+$ ATM isolation

VAT was dissected from young (3-month-old) or aged (24-month-old) male mice, and SVIF was isolated. Cells were incubated with anti-mouse F4/80-APC antibody (Thermo Fisher Scientific, 17-4801-82) for 30 minutes, followed by magnetic tagging through anti-APC beads (Miltenyi Biotec). After that, F4/80$^+$ ATMs were sorted through magnetic-activated cell sorting and used for the experiments.

Statistics and reproducibility

No statistical analyses were used to predetermine sample sizes, but our sample sizes are similar to those reported in previous publications[57,71,74]. For humans, all of the available samples were used. For mice, sample sizes were decided based on the previous experiments. No data were excluded from the analyses. The investigators were blinded to plasma proteomics before the downstream analysis. Otherwise, data collection and analysis were not performed blinded to the conditions of the experiments. For mouse in vivo experiments, mice were allocated by simple randomization to isotype or C3a-neutralizing antibody treatment on the day of the intra-adipose injection. Data distribution was assumed to be normal, but this was not formally tested. The exact numbers of participants and animals and statistical methods used in each experiment can be found in the figure legends. For the plasma proteomics analysis, adjusted *P* values were used. For the in vitro and in vivo experiments, a two-tailed Student's *t*-test (between the two groups) or one-way ANOVA with multiple comparisons (more than three groups) was performed. All statistical tests were performed using GraphPad Prism 9 for Windows (GraphPad Software). The exact *P* values are presented in each figure. Data are presented as mean ± s.e.m.

Reporting summary

Further information on research design is available in the Nature Portfolio Reporting Summary linked to this article.

Data availability

The raw data of plasma proteomics analysis can be found in Supplementary Table 1 and are publicly available at Zenodo (https://doi.org/10.5281/zenodo.18805277)[1]. Previously published scRNA-seq data have been deposited in the Gene Expression Omnibus under accession numbers GSE137076 and GSE180910. All other data supporting the findings of this study are available within the paper or from the corresponding author upon reasonable request. Versions of software and packages used are stated in Methods. Source data are provided with this paper.

References

1. Kim, H. H. & Dixit, V. D. Metabolic regulation of immunological aging. *Nat. Aging* **5**, 1425–1440 (2025).
2. Clark, J. P. et al. Caloric restriction reprograms adipose tissues in rhesus monkeys. *Aging Cell* **24**, e70254 (2025).
3. Mattison, J. A. et al. Caloric restriction improves health and survival of rhesus monkeys. *Nat. Commun.* **8**, 14063 (2017).
4. Speakman, J. R. & Mitchell, S. E. Caloric restriction. *Mol. Aspects Med.* **32**, 159–221 (2011).
5. Spadaro, O. et al. Caloric restriction in humans reveals immunometabolic regulators of health span. *Science* **375**, 671–677 (2022).
6. Ryu, S. et al. The matricellular protein SPARC induces inflammatory interferon-response in macrophages during aging. *Immunity* **55**, 1609–1626 (2022).
7. Lee, A. H. et al. Cysteine depletion triggers adipose tissue thermogenesis and weight loss. *Nat. Metab.* **7**, 1204–1222 (2025).
8. Pinto, M. R., Melillo, D., Giacomelli, S., Sfyroera, G. & Lambris, J. D. Ancient origin of the complement system: emerging invertebrate models. *Adv. Exp. Med. Biol.* **598**, 372–388 (2007).
9. Hajishengallis, G., Reis, E. S., Mastellos, D. C., Ricklin, D. & Lambris, J. D. Novel mechanisms and functions of complement. *Nat. Immunol.* **18**, 1288–1298 (2017).
10. Wu, M. et al. Gut complement induced by the microbiota combats pathogens and spares commensals. *Cell* **187**, 897–913 (2024).
11. King, B. C. et al. Complement component C3 is highly expressed in human pancreatic islets and prevents β cell death via ATG16L1 interaction and autophagy regulation. *Cell Metab.* **29**, 202–210 (2019).
12. Mastellos, D. C., Hajishengallis, G. & Lambris, J. D. A guide to complement biology, pathology and therapeutic opportunity. *Nat. Rev. Immunol.* **24**, 118–141 (2024).
13. Coulthard, L. G. & Woodruff, T. M. Is the complement activation product C3a a proinflammatory molecule? Re-evaluating the evidence and the myth. *J. Immunol.* **194**, 3542–3548 (2015).
14. Youm, Y. H. et al. Canonical Nlrp3 inflammasome links systemic low-grade inflammation to functional decline in aging. *Cell Metab.* **18**, 519–532 (2013).
15. Fu, S. et al. Centenarian longevity is positively correlated with IgE levels but negatively correlated with C3/C4 levels, abdominal obesity and metabolic syndrome. *Cell Mol. Immunol.* **17**, 1196–1197 (2020).
16. Anderson, R. M., Le Couteur, D. G. & de Cabo, R. Caloric restriction research: new perspectives on the biology of aging. *J. Gerontol. A* **73**, 1–3 (2017).
17. Fontana, L., Partridge, L. & Longo, V. D. Extending healthy life span—from yeast to humans. *Science* **328**, 321–326 (2010).
18. Wu, X. et al. Complement C3 deficiency ameliorates aging related changes in the kidney. *Life Sci.* **260**, 118370 (2020).
19. Cribbs, D. H. et al. Extensive innate immune gene activation accompanies brain aging, increasing vulnerability to cognitive decline and neurodegeneration: a microarray study. *J. Neuroinflammation* **9**, 179 (2012).
20. Schaum, N. et al. Ageing hallmarks exhibit organ-specific temporal signatures. *Nature* **583**, 596–602 (2020).
21. Ding, Y. et al. Comprehensive human proteome profiles across a 50-year lifespan reveal aging trajectories and signatures. *Cell* **188**, 5763–5784 (2025).
22. Naito, A. T. et al. Complement C1q activates canonical Wnt signaling and promotes aging-related phenotypes. *Cell* **149**, 1298–1313 (2012).
23. Scott-Hewitt, N. et al. Microglial-derived C1q integrates into neuronal ribonucleoprotein complexes and impacts protein homeostasis in the aging brain. *Cell* **187**, 4193–4212 (2024).

24. Alper, C. A., Johnson, A. M., Birtch, A. G. & Moore, F. D. Human C'3: evidence for the liver as the primary site of synthesis. *Science* **163**, 286–288 (1969).
25. Cianflone, K. et al. Adipsin/acylation stimulating protein system in human adipocytes: regulation of triacylglycerol synthesis. *Biochemistry* **33**, 9489–9495 (1994).
26. Natoli, R. et al. Retinal macrophages synthesize C3 and activate complement in AMD and in models of focal retinal degeneration. *Invest Ophthalmol. Vis. Sci.* **58**, 2977–2990 (2017).
27. Kruglikov, I. L. & Scherer, P. E. Control of adipose tissue cellularity by the terminal complement cascade. *Nat. Rev. Endocrinol.* **19**, 679–680 (2023).
28. Goldberg, E. L. & Dixit, V. D. Drivers of age-related inflammation and strategies for healthspan extension. *Immunol. Rev.* **265**, 63–74 (2015).
29. van den Beld, A. W. et al. IGFBP-2 and aging: a 20-year longitudinal study on IGFBP-2, IGF-I, BMI, insulin sensitivity and mortality in an aging population. *Eur. J. Endocrinol.* **180**, 109–116 (2019).
30. Kim, K. S. et al. Induction of cellular senescence by insulin-like growth factor binding protein-5 through a p53-dependent mechanism. *Mol. Biol. Cell* **18**, 4543–4552 (2007).
31. Vallejo, A. N. et al. Resistance to age-dependent thymic atrophy in long-lived mice that are deficient in pregnancy-associated plasma protein A. *Proc. Natl Acad. Sci. USA* **106**, 11252–11257 (2009).
32. Nguyen, T. T. & Corvera, S. Adipose tissue as a linchpin of organismal ageing. *Nat. Metab.* **6**, 793–807 (2024).
33. Lee, S. M. et al. FABP3-mediated membrane lipid saturation alters fluidity and induces ER stress in skeletal muscle with aging. *Nat. Commun.* **11**, 5661 (2020).
34. Kivimaki, M. et al. Social disadvantage accelerates aging. *Nat. Med.* **31**, 1635–1643 (2025).
35. Lv, J. et al. Targeting FABP4 in elderly mice rejuvenates liver metabolism and ameliorates aging-associated metabolic disorders. *Metabolism* **142**, 155528 (2023).
36. Coschigano, K. T., Clemmons, D., Bellush, L. L. & Kopchick, J. J. Assessment of growth parameters and life span of GHR/BP gene-disrupted mice. *Endocrinology* **141**, 2608–2613 (2000).
37. Aging Atlas, C. Aging Atlas: a multi-omics database for aging biology. *Nucleic Acids Res.* **49**, D825–D830 (2021).
38. Oh, H. S. et al. Organ aging signatures in the plasma proteome track health and disease. *Nature* **624**, 164–172 (2023).
39. Prasse, A. et al. A vicious circle of alveolar macrophages and fibroblasts perpetuates pulmonary fibrosis via CCL18. *Am. J. Respir. Crit. Care Med.* **173**, 781–792 (2006).
40. Jancso, Z., Hegyi, E. & Sahin-Toth, M. Chymotrypsin reduces the severity of secretagogue-induced pancreatitis in mice. *Gastroenterology* **155**, 1017–1021 (2018).
41. Mao, H. et al. Protective and anti-inflammatory role of REG1A in inflammatory bowel disease induced by JAK/STAT3 signaling axis. *Int. Immunopharmacol.* **92**, 107304 (2021).
42. Chang, Y. Y. et al. Deletion of cadherin-17 enhances intestinal permeability and susceptibility to intestinal tumour formation. *J. Pathol.* **246**, 289–299 (2018).
43. Huang, J. et al. Myocardin regulates BMP10 expression and is required for heart development. *J. Clin. Invest.* **122**, 3678–3691 (2012).
44. Ashburner, M. et al. Gene Ontology: tool for the unification of biology. *Nat. Genet.* **25**, 25–29 (2000).
45. Kanehisa, M. & Goto, S. KEGG: kyoto encyclopedia of genes and genomes. *Nucleic Acids Res.* **28**, 27–30 (2000).
46. Lee, J., Seroogy, K. B. & Mattson, M. P. Dietary restriction enhances neurotrophin expression and neurogenesis in the hippocampus of adult mice. *J. Neurochem.* **80**, 539–547 (2002).
47. Spaulding, C. C., Walford, R. L. & Effros, R. B. Calorie restriction inhibits the age-related dysregulation of the cytokines TNF-α and IL-6 in C3B10RF1 mice. *Mech. Ageing Dev.* **93**, 87–94 (1997).
48. Weiss, E. P. & Fontana, L. Caloric restriction: powerful protection for the aging heart and vasculature. *Am. J. Physiol. Heart Circ. Physiol.* **301**, H1205–H1219 (2011).
49. Palma, C. et al. Caloric restriction promotes immunometabolic reprogramming leading to protection from tuberculosis. *Cell Metab.* **33**, 300–318 (2021).
50. Gaya da Costa, M. et al. Age and sex-associated changes of complement activity and complement levels in a healthy Caucasian population. *Front. Immunol.* **9**, 2664 (2018).
51. Yates, J. R. et al. Complement C3 variant and the risk of age-related macular degeneration. *N. Engl. J. Med.* **357**, 553–561 (2007).
52. Zaghlool, S. B. et al. Revealing the role of the human blood plasma proteome in obesity using genetic drivers. *Nat. Commun.* **12**, 1279 (2021).
53. West, E. E. & Kemper, C. Complosome—the intracellular complement system. *Nat. Rev. Nephrol.* **19**, 426–439 (2023).
54. Laudisi, F. et al. Cutting edge: the NLRP3 inflammasome links complement-mediated inflammation and IL-1β release. *J. Immunol.* **191**, 1006–1010 (2013).
55. Paik, S., Kim, J. K., Silwal, P., Sasakawa, C. & Jo, E. K. An update on the regulatory mechanisms of NLRP3 inflammasome activation. *Cell Mol. Immunol.* **18**, 1141–1160 (2021).
56. Goldberg, E. L. et al. IL-33 causes thermogenic failure in aging by expanding dysfunctional adipose ILC2. *Cell Metab.* **33**, 2277–2287 (2021).
57. Gonzalez-Hurtado, E. et al. Nerve-associated macrophages control adipose homeostasis across lifespan and restrain age-related inflammation. *Nat. Aging* **5**, 1828–1843 (2025).
58. Tchkonia, T., Zhu, Y., van Deursen, J., Campisi, J. & Kirkland, J. L. Cellular senescence and the senescent secretory phenotype: therapeutic opportunities. *J. Clin. Invest.* **123**, 966–972 (2013).
59. Suryadevara, V. et al. SenNet recommendations for detecting senescent cells in different tissues. *Nat. Rev. Mol. Cell Biol.* **25**, 1001–1023 (2024).
60. SenNet, C. NIH SenNet Consortium to map senescent cells throughout the human lifespan to understand physiological health. *Nat. Aging* **2**, 1090–1100 (2022).
61. Camell, C. D. et al. Inflammasome-driven catecholamine catabolism in macrophages blunts lipolysis during ageing. *Nature* **550**, 119–123 (2017).
62. Takabayashi, T. et al. A new biologic role for C3a and C3a desArg: regulation of TNF-alpha and IL-1 beta synthesis. *J. Immunol.* **156**, 3455–3460 (1996).
63. Mastellos, D. et al. Novel monoclonal antibodies against mouse C3 interfering with complement activation: description of fine specificity and applications to various immunoassays. *Mol. Immunol.* **40**, 1213–1221 (2004).
64. Davidson, S. et al. Single-cell RNA sequencing reveals a dynamic stromal niche that supports tumor growth. *Cell Rep.* **31**, 107628 (2020).
65. Mabrouk, M. et al. Afucosylated IgG promote thrombosis in mouse injected with SARS-CoV-2 spike expressing megakaryocytes. *Int. J. Mol. Sci.* **26**, 7002 (2025).
66. Hasturk, H. et al. Phase IIa clinical trial of complement C3 inhibitor AMY-101 in adults with periodontal inflammation. *J. Clin. Invest.* **131**, e152973 (2021).
67. Maekawa, T. et al. Genetic and intervention studies implicating complement C3 as a major target for the treatment of periodontitis. *J. Immunol.* **192**, 6020–6027 (2014).
68. Lamers, C. et al. Insight into mode-of-action and structural determinants of the compstatin family of clinical complement inhibitors. *Nat. Commun.* **13**, 5519 (2022).

69. Zhang, Y. et al. The starvation hormone, fibroblast growth factor-21, extends lifespan in mice. *eLife* **1**, e00065 (2012).
70. Youm, Y. H., Horvath, T. L., Mangelsdorf, D. J., Kliewer, S. A. & Dixit, V. D. Prolongevity hormone FGF21 protects against immune senescence by delaying age-related thymic involution. *Proc. Natl Acad. Sci. USA* **113**, 1026–1031 (2016).
71. Ryu, S. et al. Reduction of SPARC protects mice against NLRP3 inflammasome activation and obesity. *J. Clin. Invest.* **133**, e169173 (2023).
72. Zeng, W. et al. Saponins isolated from *Radix polygalae* extent lifespan by modulating complement C3 and gut microbiota. *Pharmacol. Res.* **170**, 105697 (2021).
73. Huffman, D. M. & Barzilai, N. Role of visceral adipose tissue in aging. *Biochim. Biophys. Acta* **1790**, 1117–1123 (2009).
74. Youm, Y. H. et al. Enhanced paracrine action of FGF21 in stromal cells delays thymic aging. *Nat. Aging* **5**, 576–587 (2025).
75. Gliniak, C. M. et al. FGF21 promotes longevity in diet-induced obesity through metabolic benefits independent of growth suppression. *Cell Metab.* **37**, 1547–1567 (2025).
76. Zheng, R. et al. The complement system, aging, and aging-related diseases. *Int. J. Mol. Sci.* **23**, 8689 (2022).
77. Liao, D. S. et al. Complement C3 inhibitor pegcetacoplan for geographic atrophy secondary to age-related macular degeneration: a randomized phase 2 trial. *Ophthalmology* **127**, 186–195 (2020).
78. Ritchie, M. E. et al. limma powers differential expression analyses for RNA-sequencing and microarray studies. *Nucleic Acids Res.* **43**, e47 (2015).
79. Korotkevich, G. et al. Fast gene set enrichment analysis. Preprint at *bioRxiv* https://doi.org/10.1101/060012 (2021).
80. Huber, W., von Heydebreck, A., Sultmann, H., Poustka, A. & Vingron, M. Variance stabilization applied to microarray data calibration and to the quantification of differential expression. *Bioinformatics* **18**, S96–S104 (2002).
81. Kim, H. H. et al. Raw values for plasma SOMAScan data of CALERIE participants at baseline and 2 years after caloric restriction. *Zenodo* https://doi.org/10.5281/zenodo.18805277 (2026).

Acknowledgements

We thank all investigators and staff who coordinated and executed the CALERIE-II clinical trial. This study was supported, in part, by National Institutes of Health grants AG073969, P01AG051459 and U54AG079759 (to V.D.D.).

Author contributions

M.M. conducted western blot analysis, in vitro experiments with BMDMs and in vivo experiments with mice; prepared figures; and wrote the first draft of the paper. H.-H.K. analyzed the human plasma proteomics data, in vitro experiments with ATMs and in vivo experiments with mice; prepared and arranged figures; and wrote the first draft of the paper. Y.-H.Y. and T.D. helped with in vivo experiments with C3a-neutralizing antibody, prepared the materials for the proteomics analyses and organized the clinical information of participants. E.G.-H. assisted with mouse experiments. K.Z. and M.N.A. performed the initial analysis of the human plasma proteomics. I.S. and M.N.A. analyzed the scRNA-seq analysis of the VAT SVIF. C.G. and P.E.S. participated in adipose complement experiments, including providing transgenic mice and tissue samples. S.M. and A.C.S. collected and provided human samples for the C3 ELISA. E.R. was involved in the design and execution of the CALERIE-II trial and was the principal investigator of the Pennington Biomedical Research Center site of CALERIE. V.D.D. conceived of the project, helped with data interpretation and wrote the paper.

Competing interests

The authors declare no competing interests.

Additional information

Extended data is available for this paper at https://doi.org/10.1038/s43587-026-01107-0.

Supplementary information The online version contains supplementary material available at https://doi.org/10.1038/s43587-026-01107-0.

Correspondence and requests for materials should be addressed to Vishwa Deep Dixit.

Peer review information *Nature Aging* thanks Lunzhi Dai, Andrew Greenberg and the other, anonymous, reviewer(s) for their contribution to the peer review of this work.

Reprints and permissions information is available at www.nature.com/reprints.

Publisher's note Springer Nature remains neutral with regard to jurisdictional claims in published maps and institutional affiliations.

[1]Department of Pathology, Yale School of Medicine, New Haven, CT, USA. [2]Department of Immunobiology, Yale School of Medicine, New Haven, CT, USA. [3]Department of Comparative Medicine, Yale School of Medicine, New Haven, CT, USA. [4]Department of Pathology and Immunology, Washington University School of Medicine, St. Louis, MO, USA. [5]Touchstone Diabetes Center, University of Texas Southwestern Medical Center, Dallas, TX, USA. [6]Pennington Biomedical Research Center, Baton Rouge, LA, USA. [7]Department of Internal Medicine, Yale School of Medicine, New Haven, CT, USA. [8]Yale Center for Research on Aging, Yale School of Medicine, New Haven, CT, USA. [9]These authors contributed equally: Manish Mishra, Hee-Hoon Kim. ✉e-mail: vishwa.dixit@yale.edu

https://doi.org/10.1038/s43587-026-01107-0

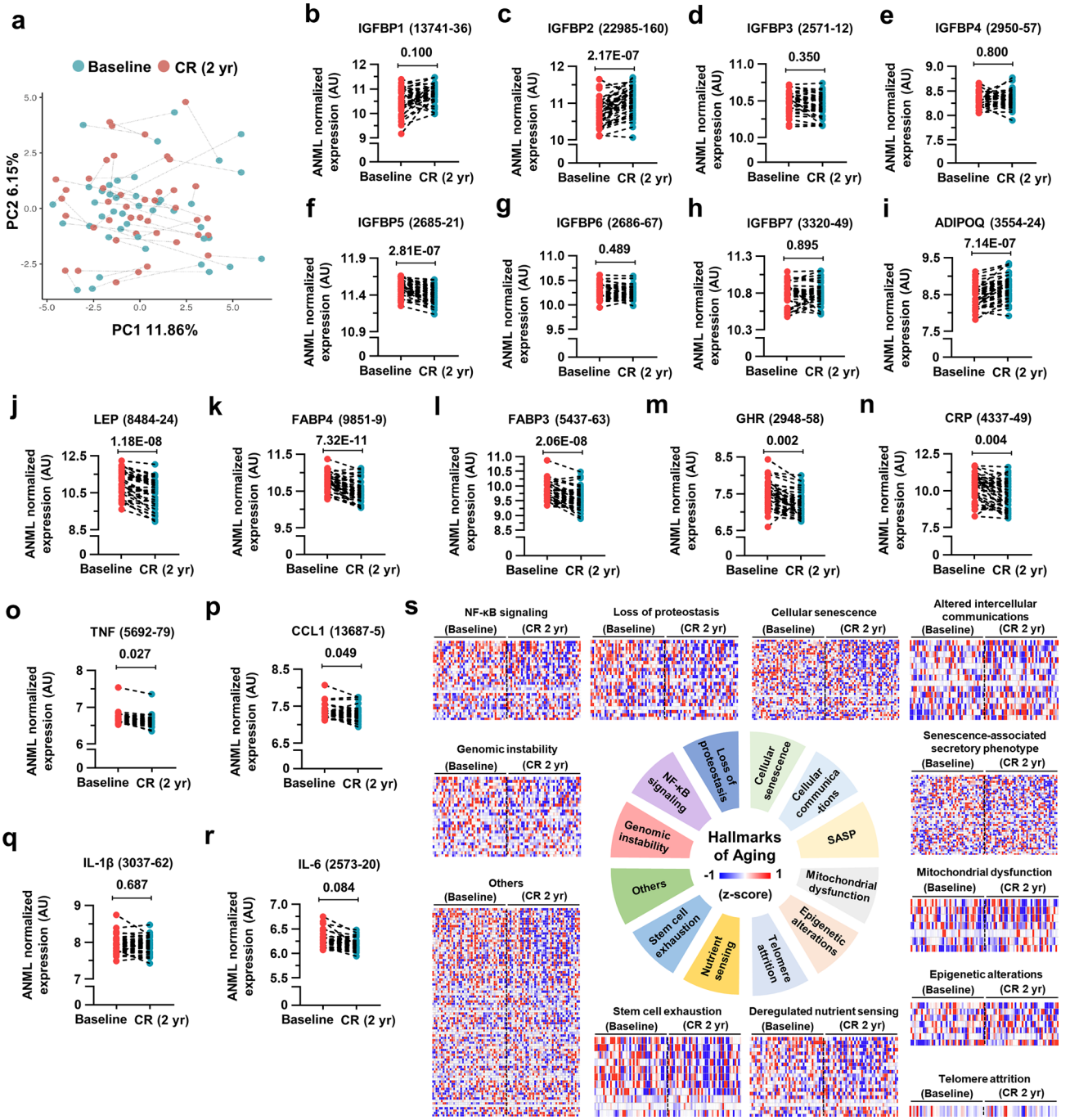

Extended Data Fig. 1 | CR in healthy individuals increases IGFBP2 and adiponectin but reduces leptin, FABPs, and inflammatory molecules in plasma. (**a**-**s**) SomaScan 7 K proteomics was performed on plasma from healthy individuals at baseline and 2 years after 14% caloric restriction (CR) ($n = 42$/group, biological replicates). (**a**) PCA plot. (**b**-**r**) The CR-mediated effects on the normalized expression levels of the indicated protein with SOMAmer ID. Paired two-tailed t-tests were performed, and exact adjusted p-values were presented. (**s**) CR-associated changes in 12 hallmarks of aging pathways were analyzed, and heatmaps for each pathway were presented.

https://doi.org/10.1038/s43587-026-01107-0

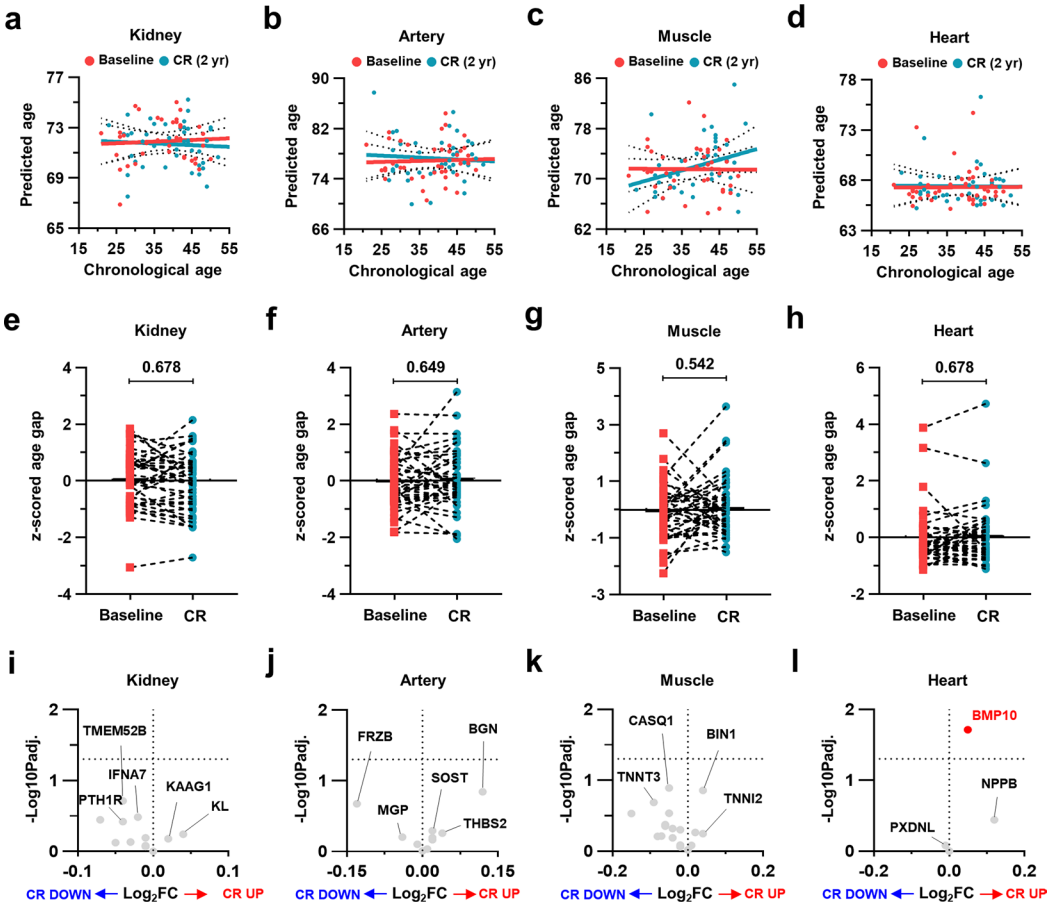

Extended Data Fig. 2 | CR does not affect the proteomic aging of the kidney, artery, muscle, and heart. (**a**-**l**) Organ-specific aging signatures were analyzed based on the plasma proteome. (**a**-**d**) Linear regression analysis was performed to compare the predicted proteomic age before and after CR in the kidney (**a**), artery (**b**), muscle (**c**), and heart (**d**). (**e**-**h**) Organ age gap was analyzed in the kidney (**e**), lung (**f**), pancreas (**g**), and intestine (**h**) ($n = 42$/group, biological replicates). Paired two-tailed t-tests were performed, and exact adjusted p-values were presented. (**i**-**l**) Volcano plots for the organ-specific proteins in the kidney (**i**), artery (**j**), muscle (**k**), and heart (**l**).

https://doi.org/10.1038/s43587-026-01107-0

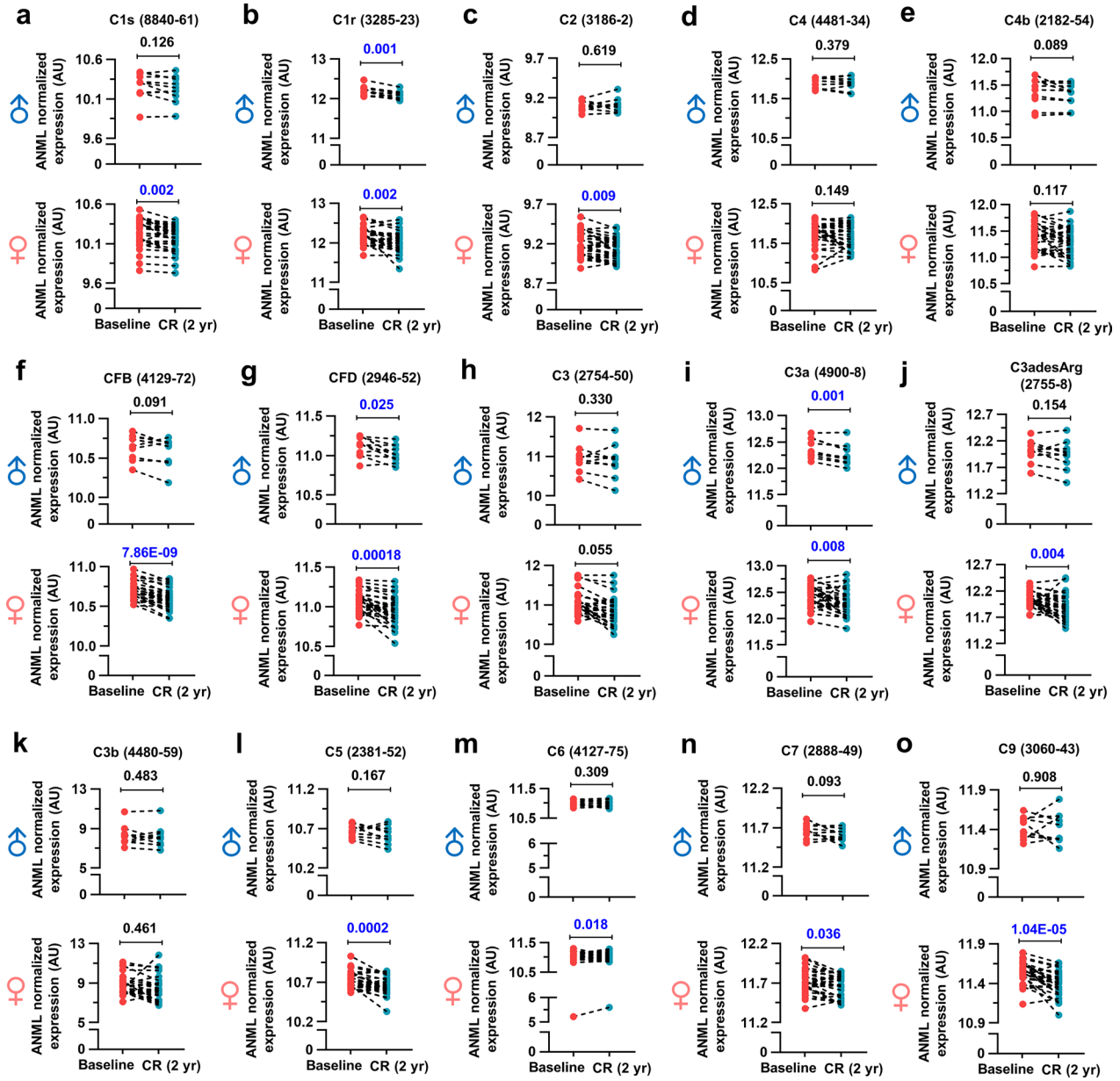

Extended Data Fig. 3 | CR reduces plasma C3a expression in both sexes. (**a**-**o**) Plasma proteomics analysis of complement components by sex (n = 42/group, biological replicates). C1s (**a**), C1r (**b**), C2 (**c**), C4 (**d**), C4b (**e**), CFB (**f**), CFD (**g**), C3 (**h**), C3a (**i**), C3adesArg (**j**), C3b (**k**), C5 (**l**), C6 (**m**), C7 (**n**), and C9 (**o**) were analyzed.

https://doi.org/10.1038/s43587-026-01107-0

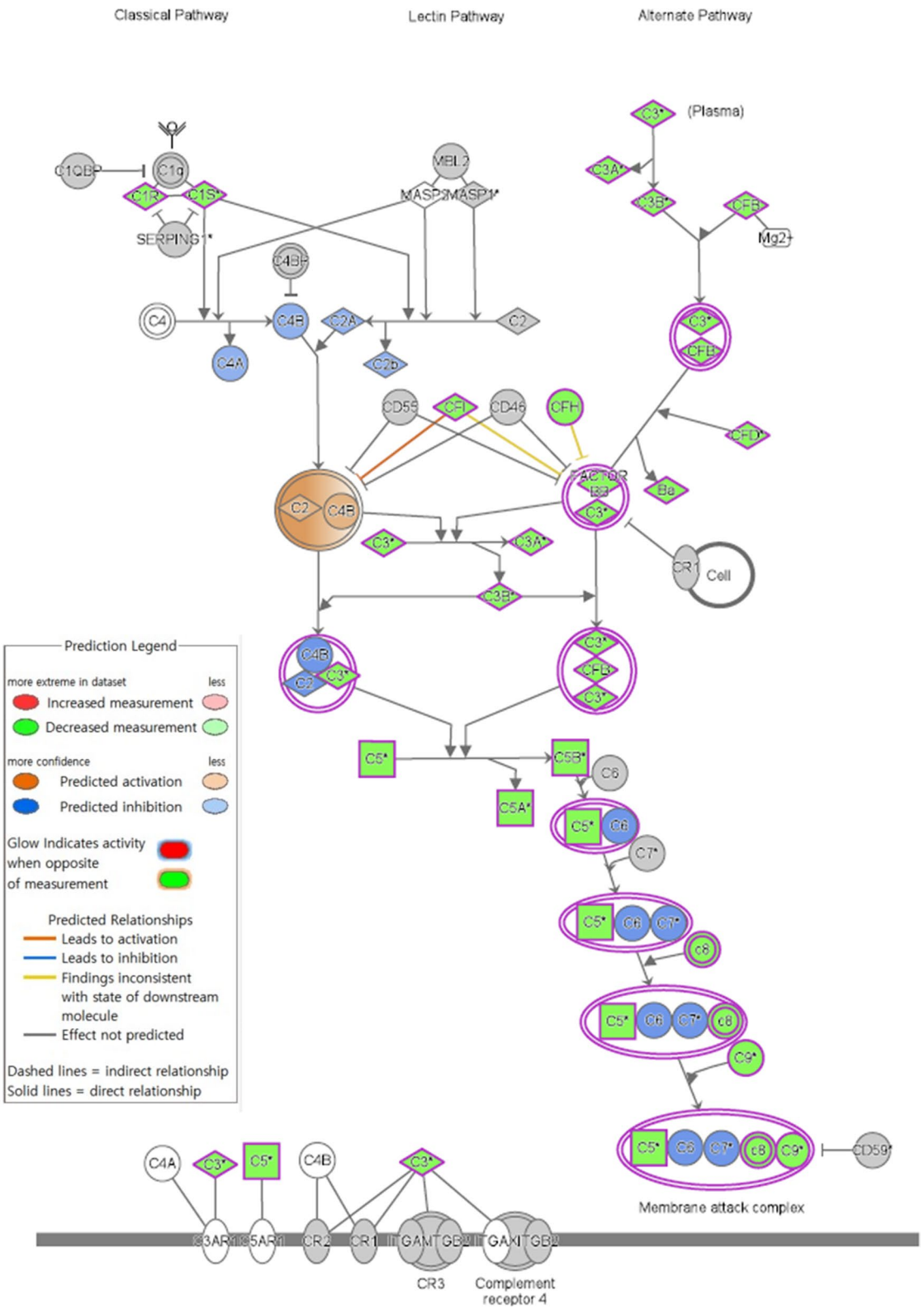

Extended Data Fig. 4 | CR in healthy individuals dampens complement pathways. The plasma proteome-based prediction for CR-induced changes in the complement system by Ingenuity Pathway Analysis. CR downregulated most components of the complement system.

https://doi.org/10.1038/s43587-026-01107-0

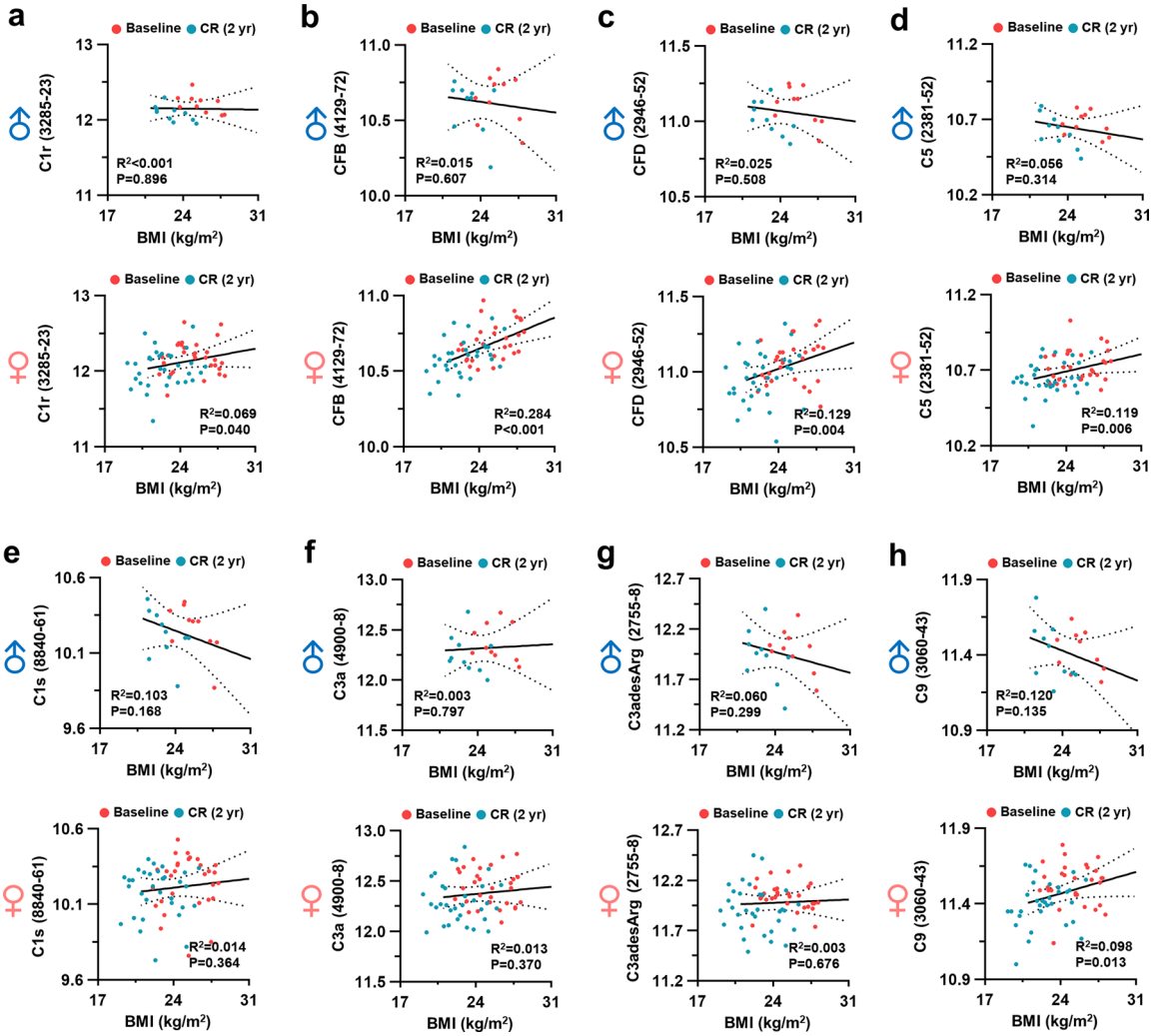

Extended Data Fig. 5 | CR-induced reduction in C3a levels is BMI-independent in both sexes. (**a**-**h**) The association of BMI and plasma levels of complement components was analyzed by sex. C1r (**a**), CFB (**b**), CFD (**c**), C5 (**d**), C1s (**e**), C3a (**f**), C3adesArg (**g**), and C9 (**h**) were analyzed.

https://doi.org/10.1038/s43587-026-01107-0

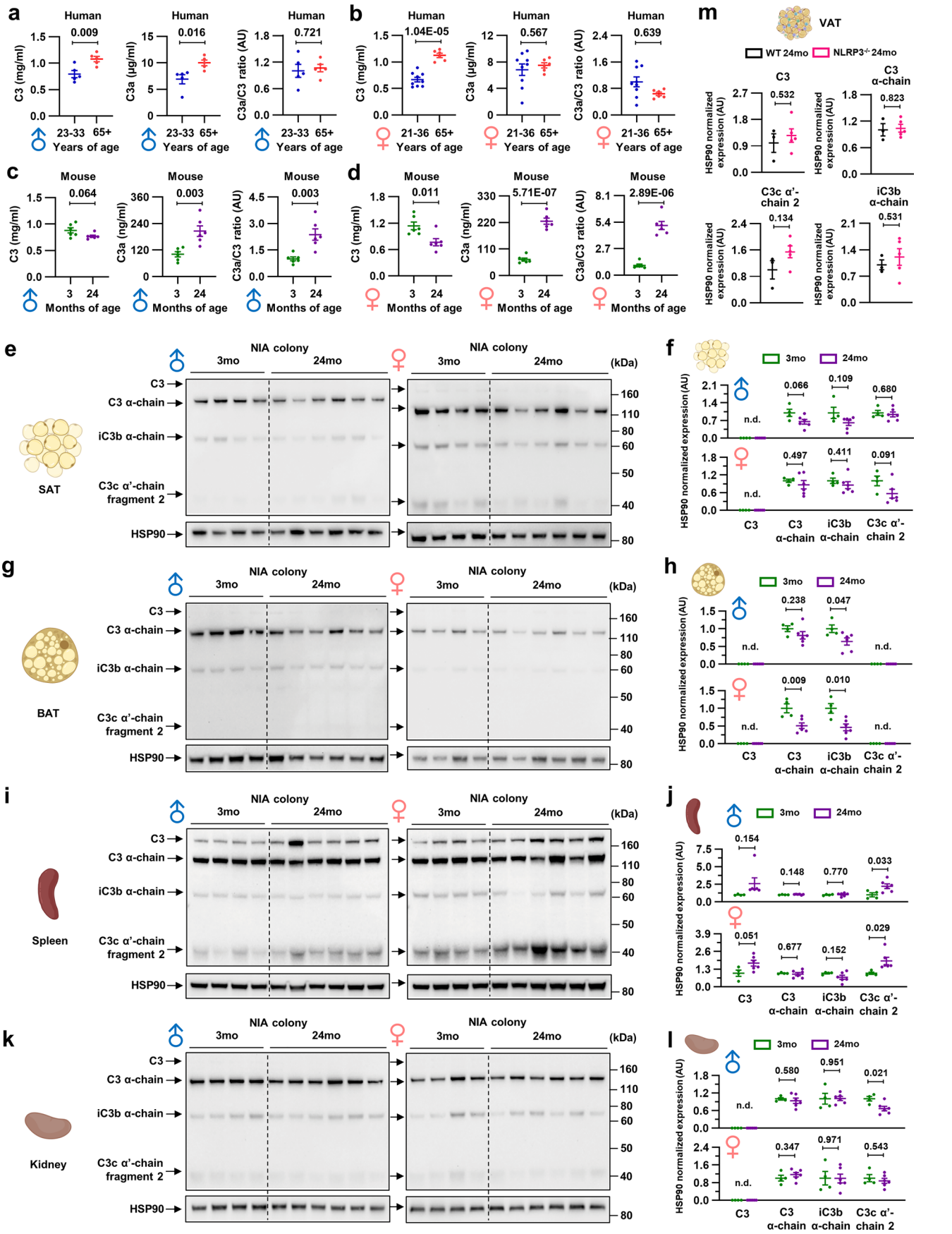

Extended Data Fig. 6 | See next page for caption.

https://doi.org/10.1038/s43587-026-01107-0

Extended Data Fig. 6 | Age-associated increase in C3a was not derived from SAT, BAT, spleen, or kidney in mice. (**a**,**b**) Human serum samples from male (**a**) or female (**b**) healthy volunteers were analyzed for C3 and C3a ELISA, and the C3a/C3 ratio was calculated (n = 5/group for males, n = 9 for 21-26 years-old females, and n = 6 for >65 years-old females, biological replicates). (**c**,**d**) Mouse serum samples from males (**c**) or females (**c**) were analyzed for C3 and C3a ELISA, and the C3a/C3 ratio was calculated (n = 6/group, biological replicates). (**e**-**l**) Representative C3 western blot analysis of the various mouse tissues (n = 4 for 3-month-old and n = 6 for 24-month-old in both sexes, biological replicates). (**e**,**f**) C3 western blot analysis of mouse subcutaneous adipose tissues (SAT). (**e**) Representative blots for C3 in both sexes. (**f**) Densitometry analysis of male (top) and female (bottom) mice. (**g**,**h**) C3 western blot analysis of mouse brown adipose tissues (BAT). (**g**) Representative blots for C3 in both sexes. (**h**) Densitometry analysis of male (top) and female (bottom) mice. (**i**,**j**) C3 western blot analysis of mouse spleen. (**i**) Representative blots for C3 in both sexes. (**j**) Densitometry analysis of male (top) and female (bottom) mice. (**k**,**l**) C3 western blot analysis of mouse kidney. (**k**) Representative blots for C3 in both sexes. (**l**) Densitometry analysis of male (top) and female (bottom) mice. (**m**) Densitometry analysis of the VAT of 24-month-old WT and NLRP3$^{-/-}$ mice (n = 3/group, biological replicates). Unpaired two-tailed t-tests were performed, and exact p-values were presented. Data presented as mean ± SEM.

https://doi.org/10.1038/s43587-026-01107-0

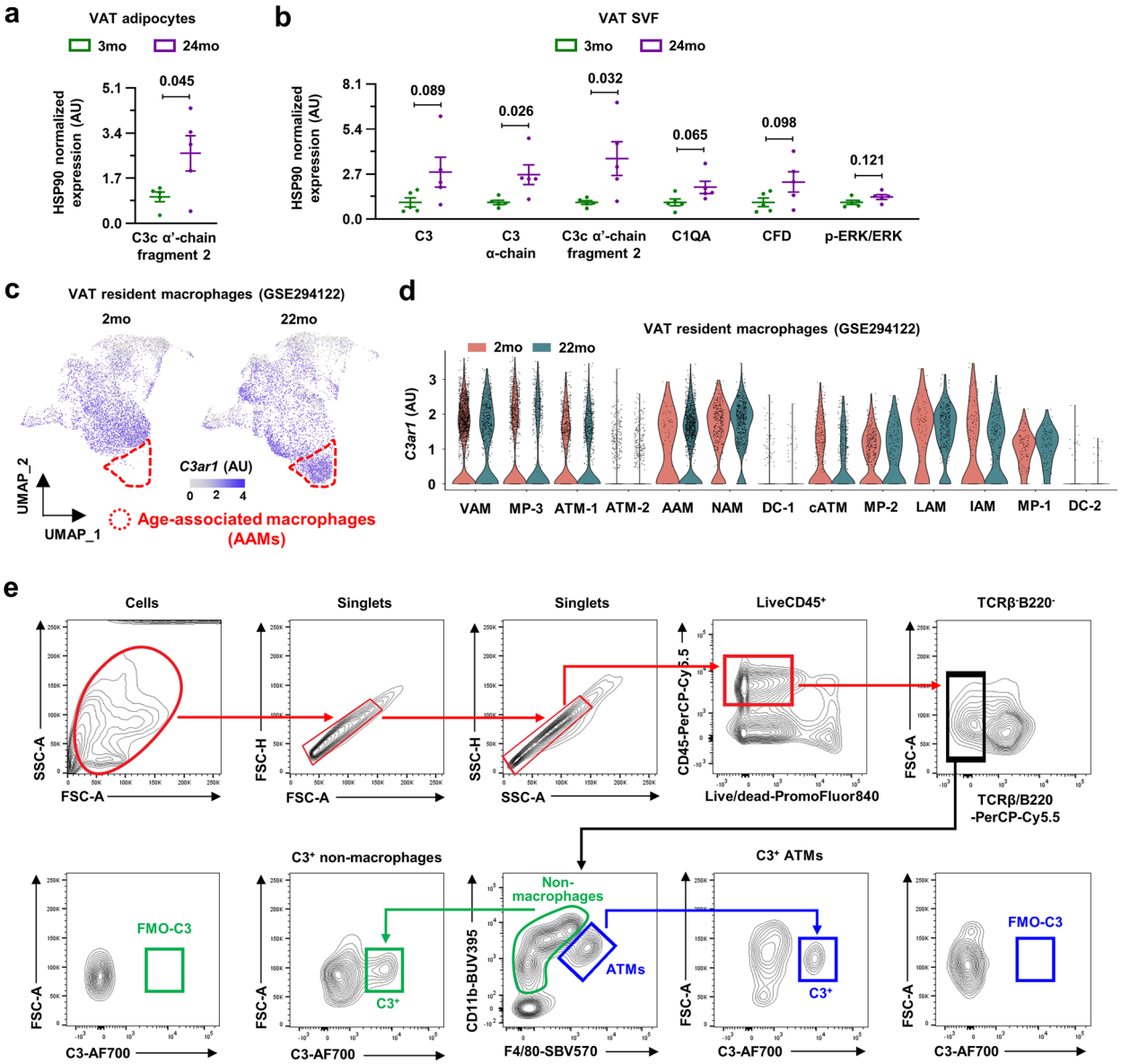

Extended Data Fig. 7 | Age-associated complement activation in the VAT occurs in the non-adipocyte fraction. (**a**) Densitometry analysis of the VAT adipocyte ($n = 5$/group, biological replicates). (**b**) Densitometry analysis of VAT SVF ($n = 5$/group, biological replicates). (**c**,**d**) VAT-resident macrophage subsets were analyzed by single-cell RNA sequencing (GSE294122). Feature plot (**c**) and violin plot (**d**) for *C3ar1* expression. (**e**) Gating strategy for analyzing C3-expressing F4/80$^+$CD11b$^+$ ATMs and F4/80$^-$CD11b$^+$ non-macrophage fractions in the VAT, along with fluorescence minus one (FMO) control for C3. Unpaired two-tailed t-tests were performed, and exact p-values were presented. Data presented as mean ± SEM.

https://doi.org/10.1038/s43587-026-01107-0

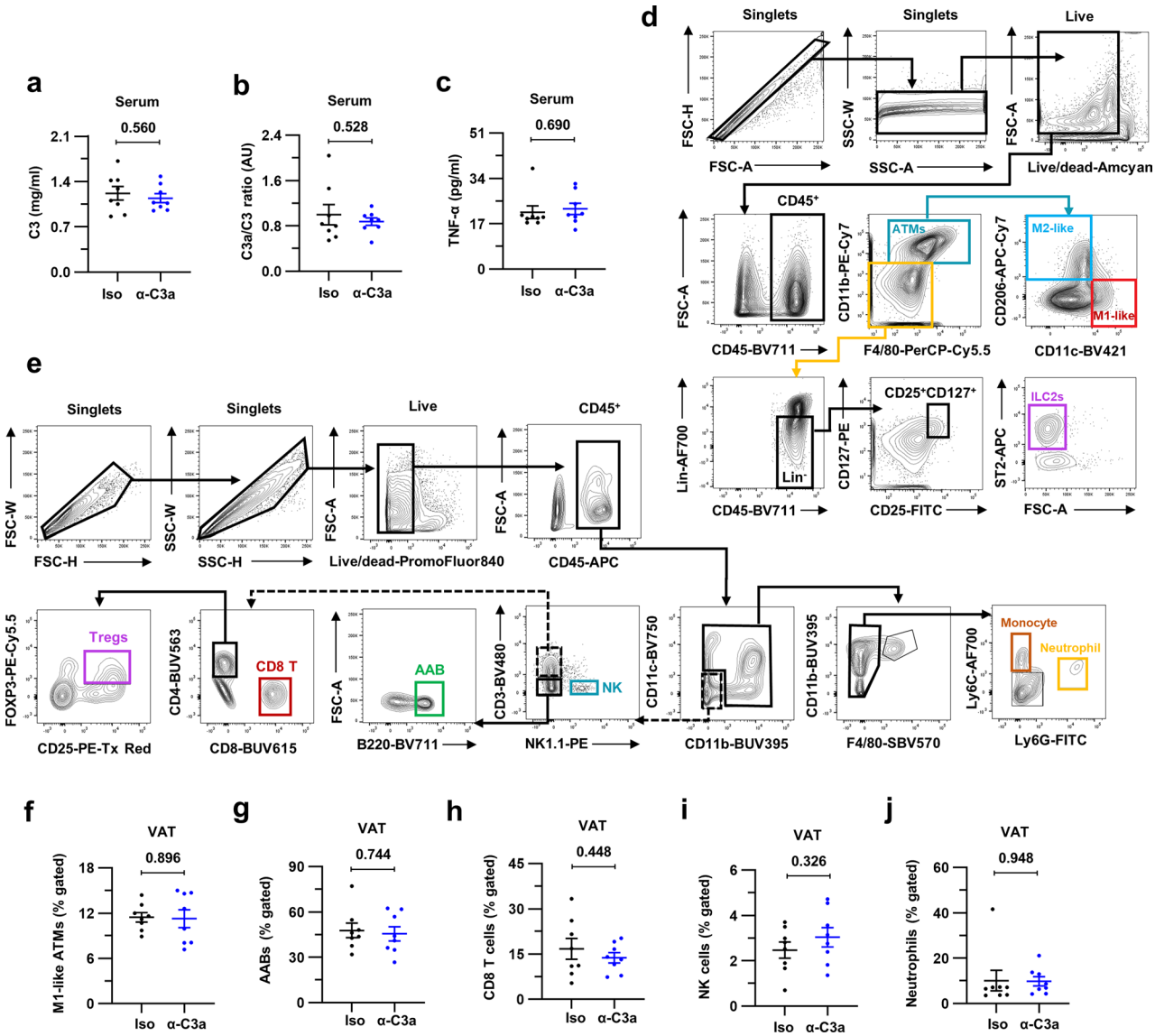

Extended Data Fig. 8 | The effects of C3a neutralization in VAT on systemic and cellular inflammaging markers. (**a**-**j**) WT 20-month-old male mice were administered either an isotype control or anti-C3a neutralizing antibody in VAT (4 μg/depot), and sacrificed after 3 days (n = 8/group, biological replicates). (**a**) Serum C3 levels. (**b**) The C3a/C3 ratio based on serum ELISA. (**c**) Serum TNF-α levels. (**d**,**e**) Flow cytometry gating strategies for ATMs and ILC2s (**d**) and lymphocytes and granulocytes (**e**). (**f**-**j**) Flow cytometry analysis of the frequencies of VAT M1-like ATMs (**f**), AABs (**g**), CD8 T cells (**h**), NK cells (**i**), and neutrophils (**j**). Unpaired two-tailed t-tests were performed, and exact p-values were presented. Data presented as mean ± SEM.

https://doi.org/10.1038/s43587-026-01107-0

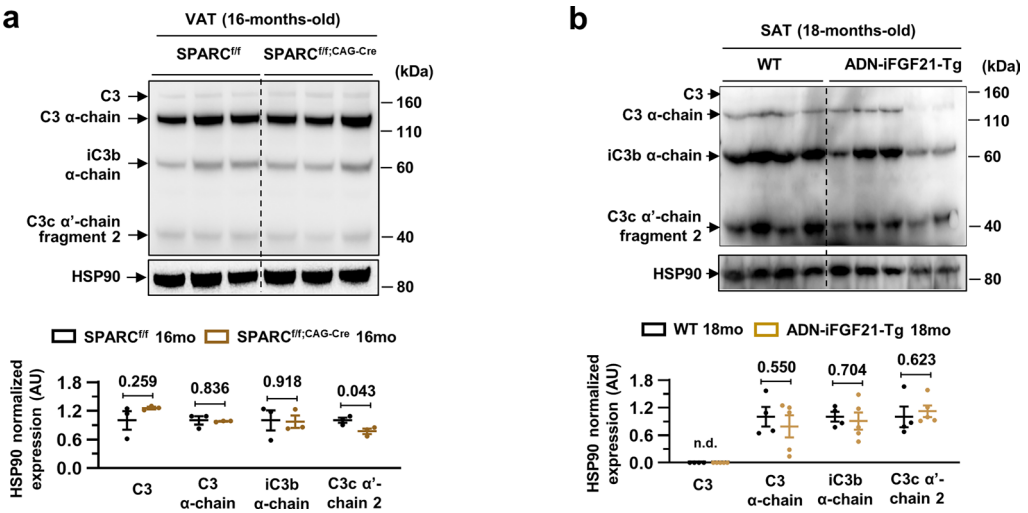

Extended Data Fig. 9 | C3 cleavage in SPARC-depleted and adipocyte-specific FGF21 overexpressed mice during aging. (**a**) Representative C3 western blot analysis of the VAT of 16-month-old SPARC$^{f/f}$ and SPARC$^{f/f;CAG-Cre}$ mice ($n = 3$/group, biological replicates). (**b**) Representative C3 western blot analysis of the SAT of 18-month-old WT ($n = 4$, biological replicates) and adipocyte-specific FGF21 overexpressed (ADN-iFGF21-Tg; $n = 5$, biological replicates) mice with densitometry analysis. Unpaired two-tailed t-tests were performed, and exact p-values were presented. Data presented as mean ± SEM.

https://doi.org/10.1038/s43587-026-01107-0

Extended Data Table 1 | Clinical characteristics of CALERIE trial participants for whom serum samples were used for proteomics

Variables	Mean ± s.e.m. or percentage		
	Baseline (n = 42)	CR 2 years (n = 42)	P value
Male (%)	23.8		N/A
White (%)	71.4		N/A
Asian (%)	4.76		N/A
Black or African American (%)	19.0		N/A
Age (years)	38.29±1.22	40.27±1.22	<0.001
Body weight (kg)	71.55±1.40	63.81±1.38	<0.001
Body mass index	25.34±0.28	22.60±0.29	<0.001
Mean waist circumference (cm)	81.43±1.27	75.32±1.23	<0.001
Fat mass (kg)	24.36±0.72	19.14±0.72	<0.001
Whole body fat (%)	71.55±1.40	63.81±1.38	<0.001
Mean systolic blood pressure (mmHg)	112.81±1.59	109.30±1.61	0.016
Mean diastolic blood pressure (mmHg)	73.84±1.12	70.4±1.21	<0.001
Serum IL-6 (pg/ml)	1.61±0.18	1.43±0.29	0.648
Serum TNF-α (pg/ml)	3.06±0.15	2.57±0.14	0.004
Serum CRP (mg/dl)	1.59±0.43	0.86±0.18	0.048
Serum leptin (ng/ml)	20.25±2.64	10.44±1.46	<0.001

Abbreviations: CR, caloric restriction; CRP, c-reactive protein; IL, interleukin; TNF, tumor necrosis factor.

nature portfolio

Corresponding author(s): Vishwa Deep Dixit

Last updated by author(s): Feb 27, 2026

Reporting Summary

Nature Portfolio wishes to improve the reproducibility of the work that we publish. This form provides structure for consistency and transparency in reporting. For further information on Nature Portfolio policies, see our Editorial Policies and the Editorial Policy Checklist.

Statistics

For all statistical analyses, confirm that the following items are present in the figure legend, table legend, main text, or Methods section.

n/a	Confirmed
☐	☒ The exact sample size (*n*) for each experimental group/condition, given as a discrete number and unit of measurement
☐	☒ A statement on whether measurements were taken from distinct samples or whether the same sample was measured repeatedly
☐	☒ The statistical test(s) used AND whether they are one- or two-sided *Only common tests should be described solely by name; describe more complex techniques in the Methods section.*
☒	☐ A description of all covariates tested
☐	☒ A description of any assumptions or corrections, such as tests of normality and adjustment for multiple comparisons
☐	☒ A full description of the statistical parameters including central tendency (e.g. means) or other basic estimates (e.g. regression coefficient) AND variation (e.g. standard deviation) or associated estimates of uncertainty (e.g. confidence intervals)
☐	☒ For null hypothesis testing, the test statistic (e.g. *F*, *t*, *r*) with confidence intervals, effect sizes, degrees of freedom and *P* value noted *Give P values as exact values whenever suitable.*
☒	☐ For Bayesian analysis, information on the choice of priors and Markov chain Monte Carlo settings
☒	☐ For hierarchical and complex designs, identification of the appropriate level for tests and full reporting of outcomes
☐	☒ Estimates of effect sizes (e.g. Cohen's *d*, Pearson's *r*), indicating how they were calculated

Our web collection on statistics for biologists contains articles on many of the points above.

Software and code

Policy information about availability of computer code

Data collection	Proteomics data was generated by SomaScan 7K platform. BD Symphony was used to collect flow cytometry data with DIVA software (v8.0.1). Western blots were developed in a Bio-Rad ChemiDoc. qRT-PCR data was collected with Roche LightCycler 480 version 1.5.0 SP3. ELISA data was collected with Varioskan LUX microplate reader (Thermo).
Data analysis	Somascan assay data were normalized following SomaLogic's pipeline. The median signal normalization was conducted using Adaptive Normalization by Maximum Likelihood (ANML) for plasma. For differential expression of proteins, ANML normalized values were log2-transformed and the values were fitted linear models using the limma R package (v 3.56.2), including donor as a blokcing factor for paired testing. The 'organage' package was used to predict the proteomic aging clock of each organ. Pathway enrichment analysis was conducted with the fgsea R package (v 1.26.0), using the limma t-statistic as the ranking metric. Volcano plot was generated with ggplot2 (v 3.5.1). For principle component analysis (PCA), expression values were normalized with vsn R package (v 3.68.0), after which PCA was performed with the base R prcomp function and visualized in ggplot2 (v 3.5.1). R version 4.3.0 was used for all the analyses. Flow cytometry data were analyzed using Flowjo 10.10. Prism version 8.0.2 (GraphPad) was used for statistical analysis.

For manuscripts utilizing custom algorithms or software that are central to the research but not yet described in published literature, software must be made available to editors and reviewers. We strongly encourage code deposition in a community repository (e.g. GitHub). See the Nature Portfolio guidelines for submitting code & software for further information.

Data

Policy information about availability of data

All manuscripts must include a data availability statement. This statement should provide the following information, where applicable:

- Accession codes, unique identifiers, or web links for publicly available datasets
- A description of any restrictions on data availability
- For clinical datasets or third party data, please ensure that the statement adheres to our policy

The raw data of plasma proteomics analysis can be found in Supplementary Table 1 and are publicly available at Zenodo (doi:10.5281/zenodo.18805277). Previously published single-cell RNA sequencing data have been deposited in the Genome Expression Omnibus under accession numbers GSE137076 and GSE180910. All other data supporting the findings of this study are available within the paper or from the corresponding author upon reasonable request. Versions of software and packages used are stated in the methods section.

Research involving human participants, their data, or biological material

Policy information about studies with human participants or human data. See also policy information about sex, gender (identity/presentation), and sexual orientation and race, ethnicity and racism.

Reporting on sex and gender	For caloric restriction clinical trial and proteomics, both men (n=10) and women (n=32) have been included.
Reporting on race, ethnicity, or other socially relevant groupings	For race, 71.4% of participants are white (n=30), 4.76% are Asian (n=2), 19.0% are black or African American (n=8), and 4.76% are unknown (n=2).
Population characteristics	Mens were aged 26 to 50 years old and womens were 22 to 48 years old at baseline, with a body mass index ranges from 22 to 28. General characteristics of participants are listed in Extended Data Table 1. The full trial protocol is available: https://clinicaltrials.gov/study/NCT00427193
Recruitment	The overall inclusion criteria detailed on https://clinicaltrials.gov/study/NCT00427193. Non-obese healthy individuals that fulfill this criteria were recruited for the study.
Ethics oversight	All clinical studies were performed under the approval guidelines by the Institutional Review Board at Pennington or Yale. The written informed consent was obtained from all participants. The full trial protocol is available: https://clinicaltrials.gov/study/NCT00427193

Note that full information on the approval of the study protocol must also be provided in the manuscript.

Field-specific reporting

Please select the one below that is the best fit for your research. If you are not sure, read the appropriate sections before making your selection.

☒ Life sciences ☐ Behavioural & social sciences ☐ Ecological, evolutionary & environmental sciences

For a reference copy of the document with all sections, see nature.com/documents/nr-reporting-summary-flat.pdf

Life sciences study design

All studies must disclose on these points even when the disclosure is negative.

Sample size	Sample size were based on power calculations from previous experiments and experiences.
Data exclusions	No data points were excluded from the study.
Replication	Plasma proteomics was performed once with n=42 per group. All experiments were independently performed at least three times giving similar results.
Randomization	Mice were allocated by simple randomization to respective groups for all experiments.
Blinding	Investigators were blinded for proteomics data generation. Otherwise, investigators were not blinded to ensure the correct injection of reagents.

Reporting for specific materials, systems and methods

We require information from authors about some types of materials, experimental systems and methods used in many studies. Here, indicate whether each material, system or method listed is relevant to your study. If you are not sure if a list item applies to your research, read the appropriate section before selecting a response.

Materials & experimental systems

n/a	Involved in the study
☐	☒ Antibodies
☒	☐ Eukaryotic cell lines
☒	☐ Palaeontology and archaeology
☐	☒ Animals and other organisms
☐	☒ Clinical data
☒	☐ Dual use research of concern
☒	☐ Plants

Methods

n/a	Involved in the study
☒	☐ ChIP-seq
☐	☒ Flow cytometry
☒	☐ MRI-based neuroimaging

Antibodies

Antibodies used

BioXcell:
Rat IgG2a isotype control (#BE0089)

Hycult biotech:
Mouse C3a (clone 3/11, #HM1072)

Abcam:
Complement C3 (clone EPR19394, #ab200999)
C1QA (polyclonal, #ab155052)

R&D Systems:
Factor-D/Adhipsin (clone 577620, #MAB5430-SP)

Cell Signaling:
p-STAT3 (Tyr705) (clone D3A7, #9145)
STAT3 (clone 79D7, #4904)
p-Erk (Thr202/Tyr204) (clone 197G2, #4377)
Erk (clone 137F5, #4695)
β-actin (#4967)

Proteintech:
HSP90 (clone 3F11C1, #60318-1-lg)

Bio-Rad:
F4/80-StarBrightViolet570 (clone CI:A3-1, #MCA497)

Novus Biologicals:
C3-AF700 (clone 11H9, #NB200-540)

Thermo Fisher:
CD16/CD32 (clone 93, #14-0161-86)
NK1.1-PE (clone PK136, #12-5941-82)
CD11b-PE-Cy7 (clone M1/70, #25-0112-82)
CD206-APC-Cy7 (clone MR6F3, #47-2061-82)
ST2-APC (clone RMST2-2, #17-9335-82)
CD45-APC (clone 30-F11, #17-0451-83)
Foxp3-PE-Cy5.5 (clone FJK-16s, #35-5773-82)

Biolegend:
CD11c-BV750 (clone N418, #117357)
B220-BV711 (clone RA3-6B2, #103255)
TCRβ-PerCP/Cyanine 5.5 (clone H57-597, #109227)
CD45R/B220-PerCP/Cyanine 5.5 (clone RA3-6B2, #103236)
CD45-BV711 (clone 30-F11, #103147)
F4/80-PerCP-Cy5.5 (clone BM8, #123128)
CD11c-BV421 (clone N418, #117329)
CD25-FITC (clone 3C7, #101908)
CD5-AF700 (clone 53-7.3, #100636)
TER-119-AF700 (clone TER-119, #116220)
Gr1-AF700 (clone RB6-8C5, #108422)
CD4-AF700 (clone RM4-5, #100536)
CD19-AF700 (clone 6D5, #115528)
NK1.1-AF700 (clone PK136, #108730)
FCeRIa-AF700 (clone MAR-1, #134324)
CD3-AF700 (clone 17A2, #100216)
TCRb-AF700 (clone H57-597, #109224)
Ly6C-AF700 (clone HK1.4, #128024)
Ly6G-FITC (clone 1A8, #127606)

CD45-PerCP-Cy5.5 (clone 30-F11, #103132)

BD Biosciences:
CD11b-BUV395 (Clone M1/70, #563553)
CD8a-BUV615 (Clone 53-6.7, #613004)
CD127-PE (clone SB/199, #552543)
CD25-PE-CF594 (clone PC61, #562694)
CD4-BUV563 (clone GK1.5, #612923)
CD3-BV480 (clone 17A2, #565642)

Validation

All antibodies are commercially available and they have been validated by the vendor and previous publications. Validation statements for all antibodies listed above can be found through the following links to manufacturer's website.

BioXcell:
Rat IgG2a isotype control (#BE0089) https://bioxcell.com/invivomab-rat-igg2a-isotype-control-anti-trinitrophenol-be0089?utm_source=google&utm_campaign={campaign}&utm_term=be0089&utm_medium=cpc&hsa_net=googlecpc&hsa_acc=7877010177&gad_source=1&gad_campaignid=20977182191&gbraid=0AAAADnFJzFaiT9oMM82NLVXVpCa6reOJ&gclid=Cj0KCQiAxJXJBhD_ARIsAH_JGjicl-Q8pzToS5epRoRwqisYnpy6VfnVGgEqv7-gVM-YyZkWbceqlcIaAnI-EALw_wcB

Hycult biotech:
Mouse C3a (clone 3/11, #HM1072) https://www.hycultbiotech.com/product/c3a-mouse-mab-3-11/

Abcam:
Complement C3 (clone EPR19394, #ab200999) https://www.abcam.com/en-us/products/primary-antibodies/c3-antibody-epr19394-ab200999
C1QA (polyclonal, #ab155052) https://www.abcam.com/en-us/products/primary-antibodies/c1qa-antibody-ab155052

R&D Systems:
Factor-D/Adhipsin (clone 577620, #MAB5430-SP) https://www.rndsystems.com/products/mouse-complement-factor-d-adipsin-antibody-577620_mab5430

Cell Signaling:
p-STAT3 (Tyr705) (clone D3A7, #9145) https://www.cellsignal.com/products/primary-antibodies/phospho-stat3-tyr705-d3a7-xp-rabbit-mab/9145
STAT3 (clone 79D7, #4904) https://www.cellsignal.com/products/primary-antibodies/stat3-79d7-rabbit-mab/4904
p-Erk (Thr202/Tyr204) (clone 197G2, #4377) https://www.cellsignal.com/products/primary-antibodies/phospho-p44-42-mapk-erk1-2-thr202-tyr204-197g2-rabbit-mab/4377
Erk (clone 137F5, #4695) https://www.cellsignal.com/products/primary-antibodies/p44-42-mapk-erk1-2-137f5-rabbit-mab/4695
β-actin (#4967) https://www.cellsignal.com/products/primary-antibodies/b-actin-antibody/4967

Proteintech:
HSP90 (clone 3F11C1, #60318-1-lg) https://www.ptglab.com/products/HSP90-Antibody-60318-1-Ig.htm?srsltid=AfmBOopgD47CrIGv6jEgzbRGToqmJsZ-I2jecJuQm-ebunKMbKDHXfYj

Bio-Rad:
F4/80-StarBrightViolet570 (clone CI:A3-1, #MCA497) https://www.bio-rad-antibodies.com/monoclonal/mouse-f4-80-antibody-cl-a3-1-mca497.html?f=purified

Novus Biologicals:
C3-AF700 (clone 11H9, #NB200-540) https://www.novusbio.com/products/complement-c3-antibody-11h9_nb200-540?srsltid=AfmBOoq-mtUfEkn4A0ExoQqCaNEsiJXW9ZxEl4G3JanE4676bMNjTYwJ

Thermo Fisher:
CD16/CD32 (clone 93, #14-0161-86) https://www.thermofisher.com/antibody/product/CD16-CD32-Antibody-clone-93-Monoclonal/14-0161-86
NK1.1-PE (clone PK136, #12-5941-82) https://www.thermofisher.com/antibody/product/NK1-1-Antibody-clone-PK136-Monoclonal/12-5941-82
CD11b-PE-Cy7 (clone M1/70, #25-0112-82) https://www.thermofisher.com/antibody/product/CD11b-Antibody-clone-M1-70-Monoclonal/25-0112-82
CD206-APC-Cy7 (clone MR6F3, #47-2061-82) https://www.thermofisher.com/antibody/product/CD206-MMR-Antibody-clone-MR6F3-Monoclonal/47-2061-82
ST2-APC (clone RMST2-2, #17-9335-82) https://www.thermofisher.com/antibody/product/IL-33R-ST2-Antibody-clone-RMST2-2-Monoclonal/17-9335-82
CD45-APC (clone 30-F11, #17-0451-83) https://www.thermofisher.com/antibody/product/CD45-Antibody-clone-30-F11-Monoclonal/17-0451-83
Foxp3-PE-Cy5.5 (clone FJK-16s, #35-5773-82) https://www.thermofisher.com/antibody/product/FOXP3-Antibody-clone-FJK-16s-Monoclonal/35-5773-82

Biolegend:
CD11c-BV750 (clone N418, #117357) https://www.biolegend.com/en-gb/products/brilliant-violet-750-anti-mouse-cd11c-antibody-17689
B220-BV711 (clone RA3-6B2, #103255) https://www.biolegend.com/en-gb/products/brilliant-violet-711-anti-mouse-human-cd45r-b220-antibody-9692
TCRβ-PerCP/Cyanine 5.5 (clone H57-597, #109227) https://www.biolegend.com/en-gb/products/percp-cyanine5-5-anti-mouse-tcr-beta-chain-antibody-5603
CD45R/B220-PerCP/Cyanine 5.5 (clone RA3-6B2, #103236) https://www.biolegend.com/en-gb/products/percp-cyanine5-5-anti-

mouse-human-cd45r-b220-antibody-4267
CD45-BV711 (clone 30-F11, #103147) https://www.biolegend.com/ja-jp/products/brilliant-violet-711-anti-mouse-cd45-antibody-10439
F4/80-PerCP-Cy5.5 (clone BM8, #123128) https://www.biolegend.com/en-us/products/percp-cyanine5-5-anti-mouse-f480-antibody-4303
CD11c-BV421 (clone N418, #117329) https://www.biolegend.com/en-us/products/brilliant-violet-421-anti-mouse-cd11c-antibody-7149
CD25-FITC (clone 3C7, #101908) https://www.biolegend.com/en-us/products/fitc-anti-mouse-cd25-antibody-4511
CD5-AF700 (clone 53-7.3, #100636) https://www.biolegend.com/en-us/products/alexa-fluor-700-anti-mouse-cd5-antibody-14408
TER-119-AF700 (clone TER-119, #116220) https://www.biolegend.com/en-us/products/alexa-fluor-700-anti-mouse-ter-119-erythroid-cells-antibody-3428
Gr1-AF700 (clone RB6-8C5, #108422) https://www.biolegend.com/en-us/products/alexa-fluor-700-anti-mouse-ly-6g-ly-6c-gr-1-antibody-3390
CD4-AF700 (clone RM4-5, #100536) https://www.biolegend.com/en-us/products/alexa-fluor-700-anti-mouse-cd4-antibody-3386
CD19-AF700 (clone 6D5, #115528) https://www.biolegend.com/en-us/products/alexa-fluor-700-anti-mouse-cd19-antibody-3391
NK1.1-AF700 (clone PK136, #108730) https://www.biolegend.com/en-us/products/alexa-fluor-700-anti-mouse-nk-1-1-antibody-6555
FCeRIa-AF700 (clone MAR-1, #134324) https://www.biolegend.com/en-us/products/alexa-fluor-700-anti-mouse-fcepsilonrialpha-antibody-12817
CD3-AF700 (clone 17A2, #100216) https://www.biolegend.com/en-us/products/alexa-fluor-700-anti-mouse-cd3-antibody-3375
TCRb-AF700 (clone H57-597, #109224) https://www.biolegend.com/en-us/products/alexa-fluor-700-anti-mouse-tcr-beta-chain-antibody-4537
Ly6C-AF700 (clone HK1.4, #128024) https://www.biolegend.com/en-us/products/alexa-fluor-700-anti-mouse-ly-6c-antibody-6757
Ly6G-FITC (clone 1A8, #127606) https://www.biolegend.com/en-us/products/fitc-anti-mouse-ly-6g-antibody-4775
CD45-PerCP-Cy5.5 (clone 30-F11, #103132) https://www.biolegend.com/en-us/products/percp-cyanine5-5-anti-mouse-cd45-antibody-4264

BD Biosciences:
CD11b-BUV395 (Clone M1/70, #563553) https://www.bdbiosciences.com/en-us/products/reagents/flow-cytometry-reagents/research-reagents/single-color-antibodies-ruo/buv395-rat-anti-cd11b.563553?tab=product_details
CD8a-BUV615 (Clone 53-6.7, #613004) https://www.bdbiosciences.com/en-us/products/reagents/flow-cytometry-reagents/research-reagents/single-color-antibodies-ruo/buv615-rat-anti-mouse-cd8a.613004?tab=product_details
CD127-PE (clone SB/199, #552543) https://www.bdbiosciences.com/en-us/products/reagents/flow-cytometry-reagents/research-reagents/single-color-antibodies-ruo/pe-rat-anti-mouse-cd127.552543?tab=product_details
CD25-PE-CF594 (clone PC61, #562694) https://www.bdbiosciences.com/en-us/products/reagents/flow-cytometry-reagents/research-reagents/single-color-antibodies-ruo/pe-cf594-rat-anti-mouse-cd25.562694?tab=product_details
CD4-BUV563 (clone GK1.5, #612923) https://www.bdbiosciences.com/en-us/products/reagents/flow-cytometry-reagents/research-reagents/single-color-antibodies-ruo/buv563-rat-anti-mouse-cd4.612923?tab=product_details
CD3-BV480 (clone 17A2, #565642) https://www.bdbiosciences.com/en-us/products/reagents/flow-cytometry-reagents/research-reagents/single-color-antibodies-ruo/bv480-rat-anti-mouse-cd3-molecular-complex.565642?tab=product_details

Animals and other research organisms

Policy information about studies involving animals; ARRIVE guidelines recommended for reporting animal research, and Sex and Gender in Research

Laboratory animals	Mice were on the C57BL/6J or C57BL/6N background. Young (3 to 5 months old) and aged (20 to 24 months old) wild-type male and female C57BL/6J mice were purchased from the Jackson Laboratory. All C57BL/6N mice were provided by the National Institute on Aging (NIA) aged rodent colony. All mice were maintained in a specific pathogen-free condition on a regular 12/12 dark/light cycle. For C3a-neutralizing antibody experiments, 20-month-old C57BL/6N male mice were used. For C3 inhibitor treatment experiments, 3-month-old or 20-month-old C57BL/6N male mice were used. Animal experiments and animal use was conducted in compliance with the National Institute of Health Guidelines for the Care and Use of Laboratory Animals and was approved by the Institutional Care and Use Committee at Yale University.
Wild animals	This study did not involve wild animals.
Reporting on sex	Both males and females were used in this study and clearly noted in the figures and figure legends.
Field-collected samples	This study did not involve field-collected samples.
Ethics oversight	All animal procedures were approved by the Yale Institutional Animal Care and Use Committee.

Note that full information on the approval of the study protocol must also be provided in the manuscript.

Clinical data

Policy information about clinical studies

All manuscripts should comply with the ICMJE guidelines for publication of clinical research and a completed CONSORT checklist must be included with all submissions.

Clinical trial registration	NCT00427193
Study protocol	The full trial protocol is available: https://clinicaltrials.gov/study/NCT00427193

Data collection	Participants were allocated by simple randomization to either 25% caloric restriction (CR) or ad libitum caloric intake for two years. Participants in the CR group actually reached 14% of CR. Men were between 26 and 50 years old and women were between 22 and 48 years old at baseline. The body mass index (BMI) of participants was between 22.0 to 28.0 kg/m2 at baseline. Plasma samples were collected at baseline and after 2 years of CR.
Outcomes	The overall primary, secondary, and other outcomes are listed in: https://clinicaltrials.gov/study/NCT00427193

Plants

Seed stocks	*Report on the source of all seed stocks or other plant material used. If applicable, state the seed stock centre and catalogue number. If plant specimens were collected from the field, describe the collection location, date and sampling procedures.*
Novel plant genotypes	*Describe the methods by which all novel plant genotypes were produced. This includes those generated by transgenic approaches, gene editing, chemical/radiation-based mutagenesis and hybridization. For transgenic lines, describe the transformation method, the number of independent lines analyzed and the generation upon which experiments were performed. For gene-edited lines, describe the editor used, the endogenous sequence targeted for editing, the targeting guide RNA sequence (if applicable) and how the editor was applied.*
Authentication	*Describe any authentication procedures for each seed stock used or novel genotype generated. Describe any experiments used to assess the effect of a mutation and, where applicable, how potential secondary effects (e.g. second site T-DNA insertions, mosiacism, off-target gene editing) were examined.*

Flow Cytometry

Plots

Confirm that:

☒ The axis labels state the marker and fluorochrome used (e.g. CD4-FITC).

☒ The axis scales are clearly visible. Include numbers along axes only for bottom left plot of group (a 'group' is an analysis of identical markers).

☒ All plots are contour plots with outliers or pseudocolor plots.

☒ A numerical value for number of cells or percentage (with statistics) is provided.

Methodology

Sample preparation	Visceral adipose tissue (VAT) was digested in 0.8mg/mL collagenase II (Worthington Biochemicals), 3% BSA (Sigma), 1.2mM Calcium Chloride, 1.0mM Magnesium Chloride, 0.8mM Zinc Chloride, and 1x HBSS (Life Technologies 14185-052) for 40-45 minutes in a 37°C waterbath with vigorous shaking. The Stromal Vascular Fraction (SVF) was filtered on a 100um cell strainer. Red blood cell lysis was performed using ACK lysis buffer, and cells were filtered a second time with a 70um cell strainer. One million SVF cells were used for flow cytometry staining. Cells were stained with live/dead Aqua viability dye (Invitrogen) or Viakrome 808 viability dye (Beckman Coulter) for 30 minutes, followed by Fc receptor blocking (Invitrogen) for 10 minutes and surface staining for 30 minutes with antibodies.
Instrument	Flow cytometry analysis was performed on a Becton Dickinson LSRII or Symphony instrument.
Software	Data were analyzed using FlowJo software (Treestar).
Cell population abundance	F4/80% macrophages represent approximately 15-20% of total hematopoietic cells in visceral adipose tissue.
Gating strategy	Full gating strategy are depicted in Extended Data Fig.7 and 8.

☒ Tick this box to confirm that a figure exemplifying the gating strategy is provided in the Supplementary Information.